Theses and Dissertations   1. Thesis and Dissertation Collection, all items

1993-06

Development of a LIDAR for integration with the Naval Postgraduate School Infrared Search and Target Designation (NPS-IRSTD) system

Regush, Murray Michael

Monterey, California. Naval Postgraduate School

http://hdl.handle.net/10945/39835

AD-A271 847

NAVAL POSTGRADUATE SCHOOL
Monterey, California

THESIS

NOV 04 1993

DEVELOPMENT OF A LIDAR FOR INTEGRATION WITH
THE NAVAL POSTGRADUATE SCHOOL INFRARED SEARCH
AND TARGET DESIGNATION (NPS-IRSTD) SYSTEM

by

Murray M. Regush

June 1993

Thesis Advisor: Alfred W. Cooper

93-26684

REPORT DOCUMENTATION PAGE

1. AGENCY USE ONLY *(Leave blank)*	2. REPORT DATE June 1993	3. REPORT TYPE AND DATES COVERED Master's Thesis

4. TITLE AND SUBTITLE	5. FUNDING NUMBERS
DEVELOPMENT OF A LIDAR FOR INTEGRATION WITH THE NAVAL POSTGRADUATE SCHOOL INFRARED SEARCH AND TARGET DESIGNATION (NPS-IRSTD) SYSTEM	

6. AUTHOR(S)

REGUSH MURRAY MICHAEL

7. PERFORMING ORGANIZATION NAME(S) AND ADDRESS(ES) Naval Postgraduate School Monterey, CA 93943-5000	8. PERFORMING ORGANIZATION REPORT NUMBER

9. SPONSORING/MONITORING AGENCY NAME(S) AND ADDRESS(ES) Naval Sea Systems Command Department of the Navy, Attention PEOSD-D2 3⁴ Washington, DC 20362-5011	10. SPONSORING/MONITORING AGENCY REPORT NUMBER

11. SUPPLEMENTARY NOTES

The views expressed in this thesis are those of the author and do not reflect the official policy or position of the Department of defense or the US Government.

12a. DISTRIBUTION/AVAILABILITY STATEMENT Approved for public release; distribution is unlimited.	12b. DISTRIBUTION CODE

13. ABSTRACT *(Maximum 200 words)* A lidar was designed and manufactured at the Naval Postgraduate School, Monterey, CA, to provide range information to atmospheric features, such as clouds. It is further planned to integrate the lidar with the NPS-IRSTD system at some future date. The NPS-IRSTD uses two vertical linear focal plane arrays for target detection and target direction can be determined very accurately but the system does not provide any useful range information. The lidar was proposed as the solution for this shortcoming. The lidar used a frequency-doubled Nd:YAG laser which had an energy output of 2 millijoules. The laser beam was expanded to 17.75 inches using a Dall-Kirkham telescope to operate within laser safety limitations. The theoretical analysis of the "Klett" method for the inversion of lidar returns was derived and a MATLAB program was written to demonstrate the process. A daytime and nighttime maximum range equation for the lidar was developed. The considerations for integrating the lidar with the NPS-IRSTD were listed and a solution was proposed to obtain the mean extinction coefficient along the path in the infrared spectrum using the lidar inversion extinction coefficient profile at 532 nanometers.

14. SUBJECT TERMS lidar, Nd:YAG, infrared, remote sensing, laser radar, lidar inversion.	15. NUMBER OF PAGES 103
	16. PRICE CODE

17. SECURITY CLASSIFICATION OF REPORT UNCLASSIFIED	18. SECURITY CLASSIFICATION OF THIS PAGE UNCLASSIFIED	19. SECURITY CLASSIFICATION OF ABSTRACT UNCLASSIFIED	20. LIMITATION OF ABSTRACT UL

Development of a LIDAR for Integration with the Naval Postgraduate School Infrared
Search and Target Designation (NPS-IRSTD) System

by

Murray M. Regush
Major, Canadian Armed Forces
BEng, Royal Military College of Canada, 1981

Submitted in partial fulfillment of the
requirements for the degree of

MASTER OF SCIENCE IN ELECTRICAL ENGINEERING

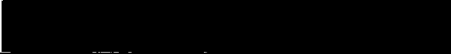from the

NAVAL POSTGRADUATE SCHOOL
June 1993

Author: _____
Murray Michael Regush

Approved By: _____
Alfred W. Cooper, Thesis Advisor

_____
John P. Powers, Thesis Co-Advisor

_____
Michael A. Morgan, Chairman of Electrical and
Computer Engineering

ABSTRACT

A lidar was designed and manufactured at the Naval Postgraduate School, Monterey, California, to provide range information regarding atmospheric features, such as clouds. It is further planned to integrate the lidar with the Naval Postgraduate School's Infrared Search and Target Designation system (NPS-IRSTD) at some future date. The NPS-IRSTD uses two vertical infrared linear focal plane arrays for target detection, and target direction can be determined very accurately but the system does not provide any useful range information. The lidar was proposed as the solution for this shortcoming. The lidar used a frequency-doubled Nd:YAG laser which had an energy output of 2 millijoules. The laser beam was expanded to 17.75 inches using a Dall-Kirkham telescope to operate within laser safety limitations. The theoretical analysis of the "Klett" method for the inversion of lidar returns was derived and a MATLAB program was written to demonstrate the process. A daytime and nighttime maximum range equation for the lidar was developed. The considerations for integrating the lidar with the NPS-IRSTD is listed and a solution is proposed to obtain the mean extinction coefficient along the path in the infrared spectrum using the lidar inversion extinction coefficient profile at 532 nanometers.

iii

TABLE OF CONTENTS

v

ACKNOWLEDGEMENT

I. INTRODUCTION

A. BACKGROUND

In January 1984, the Naval Postgraduate School (NPS) received the Advanced Development Model of the AN/SAR-8 Infrared Search and Target Designation (IRSTD) System which was then modified to bypass the background normalization circuitry and designated the NPS-IRSTD. The NPS-IRSTD is a 360-degree passive surveillance system for the detection, tracking and identification of multiple low-flying targets. The ongoing modifications to the system have been the subject of many theses and presentations in the area of real time imaging and background analysis [Ref. 1]. The NPS-IRSTD uses two linear focal plane arrays which operate in the 3 to 5 micron range but the scene image, presented after processing, does not provide any useful range information for target declaration to a combat system.

In order to provide the needed range information for target declaration, one of two approaches could be used, passive or active. One passive approach would use a three-color method and would require three separate wavelength regions from which range could be determined [Ref. 2]. The NPS-IRSTD would have to be modified with narrowband filters to provide two of the three wavebands; but, to provide the third, an additional detector array would have to be installed. An alternative passive approach would be a two-sensor triangulation but this would require an additional IRSTD [Refs. 3 and 4]. The second method would be the use of an active range-measurement device, such as a radar or laser. The laser, used in this capacity, would have an advantage over a radar because it could be directed to irradiate a specific area of interest as chosen by an NPS-IRSTD operator to obtain a target range. A disadvantage of the laser, besides being detectable by

1

the target, is that it is not an all-weather device and is severely attenuated by atmospheric losses such as fog and rain. However, this may not be as much of a problem as first thought since the NPS-IRSTD operates in the same general region as the laser and would be restricted by the same conditions.

B. RESEARCH OBJECTIVES

The use of a laser as a rangefinder is not a new concept and its capabilities extend into the radar and remote sensing fields. It would be useful at this point to introduce two new terms in order to differentiate between their uses. The term "Laser Radar" implies that the laser is used in the capacity of a radar to detect, track and image targets. The term "LIDAR", which is an acronym for LIght Detection And Ranging, implies that the laser is used for atmospheric remote sensing and the target is now on the molecular level. In both of these fields, considerable effort has been expended to understand the concepts.

The lidar, as it is presently planned for use as an adjunct to the NPS-IRSTD, will be required to provide range data to the NPS-IRSTD as well as to determine the atmospheric extinction coefficient along the path to the target. The importance of this extinction coefficient information would be realized in the image processing of the NPS-IRSTD image to correct for atmospheric propagation losses and could lead to faster target identification. Therefore, the primary objective of this thesis was to manufacture locally a lidar which, in the future, will be integrated into the NPS-IRSTD. The range and remote sensing capabilities of this lidar were studied and documented but it was intended to restrict the remote sensing capabilities to a measurement demonstration of the atmospheric extinction coefficient at this time.

2

A number of design considerations in the manufacture of the lidar were taken into account, such as wavelength, range and safety. The safety consideration was one of the driving concerns due to the operational area of the proposed lidar, which will be on top of Spanagel Hall at the Naval Postgraduate School. The use of an unsafe laser in the surrounding sky is not permitted. The subsidiary objective of this thesis was to detail all the design considerations and develop an eye-safe lidar based on materials available at the school.

The integration of the lidar into the NPS-IRSTD system was not an objective for this thesis but a preliminary system study was undertaken as a second subsidiary objective.

C. NPS-IRSTD SYSTEM OVERVIEW

The NPS-IRSTD system consists of a scanner assembly, a twelve-channel tape recorder and a 80386 computer with a frame grabber data acquisition board to provide real-time scene display. It has a field of view of 360 degrees by 10.5 degrees and operates in the 3 to 5 micron wavelength region. The system rotation rate is 0.5 Hertz and the angular location information is obtained from a position sensor mounted in the base of the scanner. An azimuthal sample width of 0.1047 milliradians is achieved using a digitization rate of 60,000 samples per revolution. [Ref. 1]

The scanner assembly consists of a 14 inch F/1 Schmidt telescope with a 10 inch entrance aperture. In the telescope's focal plane are two independent vertical linear arrays of indium antimonide (InSb) detectors. Each linear array has 90 elements and each element has an instantaneous field of view of 2.0 by 0.3 milliradians. The output signals from each 90-element array are multiplexed into six channels and are then converted into digital form for processing.

3

The digital data is fed to a twelve-channel tape recorder for storage at a data rate of 5 megabytes per second from the multiplexed 180 sensor element outputs. Real-time scene imaging is achieved by using a 80386 computer with a frame grabber data acquisition board and software developed locally. [Ref. 1]

D. LIDAR TECHNOLOGY

Lidars are used in the study of the atmosphere and the ocean. The possible atmospheric applications for lidar are the measurements of extinction profiles, major and minor gas densities, temperature and humidity profiles, wind speed, cloud composition, and pollution. The oceanic applications include measurements of surface pollution, sea surface temperature and depth. There is no one technique alone which will encompass all applications but there is, instead, a range of application-dependent approaches, such as molecular fluorescence, differential absorption, Raman or inelastic scattering, Mie/Rayleigh or elastic scattering and doppler shift. [Ref. 5]

There are a number of commercial companies which manufacture lidar systems but they are mainly designed to meet the needs of the customer's application. Therefore, it appears that the lidar is still a specialty tool which is used mainly by the scientific community.

E. DESIGNED LIDAR SYSTEM OVERVIEW

The lidar designed in this thesis was basic and limited to the determination of the distance to clouds based on measured path extinction profiles. Other lidar applications are dependent on additional technologies which were not available at the time of manufacture but may be considered for future development.

4

The designed lidar system consists of a transmitter, a receiver and electronic processing equipment. In the transmitter, a frequency-doubled Nd:YAG laser with a pulse width of 4 nanoseconds and variable energy output was used. For eye safety, the laser beam was expanded to approximately 18 inches in diameter before propagation in the atmosphere. The laser safety aspects are detailed in Chapter III. The lidar receiver consists of a lens assembly which is used to collect the backscattered laser pulse, a narrowband filter and a photomultiplier tube detector. The electronic processing equipment was not fully developed for this thesis but the output of the photomultiplier tube was observed on a digital oscilloscope, digitized and downloaded to a computer for storage. The data was later analyzed off-line to determine the atmospheric extinction coefficient.

This thesis is organized as follows:

1. Chapter II is an introduction to lidar theory and the Klett lidar inversion method.

2. Chapter III is the design of a lidar including laser safety considerations and equipment specifications.

3. Chapter IV is the analysis of the actual data obtained from the designed lidar.

4. Chapter V is the system study concerning the integration of the lidar into the NPS-IRSTD system.

5. Chapter VI is a discussion of the conclusions with recommendations for future lidar work.

6. Appendix A is the mathematical analysis upon which the Klett lidar inversion method is based.

7. Appendix B contains theoretical lidar inversions and analyses based on typical atmospheric extinction profiles using the Klett lidar inversion method.

8. Appendix C contains the detailed experimental data, the inversion computer program and the inverted atmospheric extinction coefficient profiles.

II. LIDAR THEORY

A. INTRODUCTION

Over the years, lidar has developed into a useful tool for remote sensing of the atmosphere. This has been due to the effort of many dedicated researchers and the invention of the laser. In the early 1930's, searchlights were first employed as lidars to assess the vertical density profile of the upper atmosphere using scattering techniques [Ref. 6]. The requirement for a monochromatic light source was identified when the scattering mechanisms in the atmosphere were determined to be wavelength dependent. With the invention of the laser, researchers began to realize its potential for remote sensing of the atmosphere by using previously developed searchlight techniques. Remote sensing of the atmosphere was seen to hold the possibility of fast and economical measurements compared to existing methods using weather balloons. The first actual demonstration of a working lidar appears to have been conducted in June and July 1963 by Fiocco and Smullin's use of a ruby laser to detect backscatter from the atmosphere to heights of 140 km [Ref. 7].

In its simplest form, a lidar consists of an optical transmitter, receiver and electronic processing equipment. A typical pulsed optical transmitter requires a Q-switched laser, of suitable energy output and short pulse duration, and beam expanding optics. The receiver is typically composed of a telescope to collect the backscattered laser pulse and a sensor. The electronic processing equipment mathematically transforms or inverts the time dependent output of the detector to obtain the atmospheric data. The laser and optical receiver assemblies are not necessarily mutually exclusive; there are lidars in service in which both systems share the same telescope housing.

6

B. LIDAR EQUATION

The lidar equation is the corner stone to the use of the lidar and can be derived using the Mie theory of scattering [Ref. 8]. The equation defining the backscattered power received by a lidar receiver from a pulsed laser, assuming single-scattering and omitting wavelength dependence, can be expressed as:

$$P(r) = P_0 \frac{c\tau}{2} \frac{A_0}{r^2} \beta(r) \exp\left[-2 \int_0^r \sigma(r') \, dr'\right]$$ (2-1)

where

        P(r) is the power received by the LIDAR receiver at time t,
        P_0 is the LIDAR transmitted power,
        c is the velocity of light,
        τ is the duration of the laser pulse,
        A_0 is the effective aperture of the LIDAR receiver,
        $\beta(r)$ is the atmospheric volume backscattering coefficient at range r,
        r is the range defined by $c(t-t_0)/2$, and
        $\sigma(r)$ is the atmospheric volume extinction coefficient at range r.

The atmospheric volume backscatter coefficient, $\beta(r)$, is the backscattered intensity per unit incident intensity per unit solid angle per unit path length (kilometers[-1] · steradian[-1]) and characterizes the fraction of the signal scattered back along the propagation path [Ref. 8]. $\beta(r)$ is dependent on the size parameter (which determines the type of radiative scattering), scattering efficiency and the number density of the scatterers in a given volume. The size parameter is defined as $\chi \equiv 2 \pi a /\lambda$, where λ is the wavelength of interest and a is the radius of the scattering molecule in the medium. Therefore, $\beta(r)$ is a function of the radiating wavelength and size of molecular scatterers as well as range. A $\beta(r)$ range dependence is introduced because the number density of molecular scatterers can vary along the lidar path and influence the magnitude of the backscattered laser energy. $\beta(r)$ can be approximated by neglecting the diffuse scattering by secondary scatterers,

which is equivalent to assuming that the backscattered power is primarily due to the direct scattering of the laser radiation. This is called the single scattering approximation; it may not be valid in very dense fog [Ref. 9].

The atmospheric volume extinction coefficient, $\sigma(r)$, defines the rate at which a signal attenuates as it propagates along a given path, expressed in kilometers^{-1}. $\sigma(r)$ is dependent on the absorption and scattering in the path and can be expressed in a complete form as [Ref. 10]:

$$\sigma(r,\lambda) = \kappa(r,\lambda) + B(r,\lambda,\theta) \qquad (2\text{-}2)$$

where

$\kappa(r,\lambda)$ is the atmospheric absorption coefficient, and
$B(r,\lambda,\theta)$ is the atmospheric scattering coefficient from which $\beta(r,\lambda)$ is derived.

The wavelength dependence is clearly stated in Equation (2-2), but for simplicity this dependence will be omitted due to lidar employment of near monochromatic laser light. The $\kappa(r)$ term can be further broken down as the sum of the aerosol and molecular absorption coefficients, while $B(r,\theta)$ can be rewritten as the sum of the aerosol and molecular (Mie and Rayleigh) scattering coefficients. Depending on the spectrum of interest, there are regions of dominance of various absorbers and scatterers. In the ultraviolet spectrum, the large ozone molecular $\kappa(r)$ coefficient dominates the value of $\sigma(r)$ while in the visible spectrum, $B_{aerosol}(r,\theta)$ and $B_{molecular}(r,\theta)$ strongly influence the value for $\sigma(r)$. In the infrared spectrum, $\sigma(r)$ is dominated by the various molecular absorption lines of which water and carbon dioxide are the principal absorbers; this directly produces the optical windows in this region. The range dependence is given because the number densities of the scatterers and absorbers can vary along the path as described in the discussion on $\beta(r)$. $B(r,\theta)$ can be related to $\beta(r)$ by setting the scattering observation angle, θ, to 180 degrees (backscatter).

8

It has been observed in visible and near-infrared experiments that $\sigma(r)$ is related to $\beta(r)$, assuming a homogeneous atmosphere, by the empirical power law relationship: [Ref. 11]

$$\beta(r) = \text{Constant } \sigma(r)^k \qquad (2\text{-}3)$$

where

> k is range independent but a function of the laser wavelength used and generally in the range of $1.0 \geq k \geq 0.67$, and
> *Constant* is an empirical value dependent on the properties of the scatterer irradiated.

Therefore, Equation (2-3) may not be valid in those areas of the spectrum where $\kappa(r)$ dominates or strongly influences the value for $\sigma(r)$, such as in the 8–12 micron region. This will restrict the lidar's operational spectrum and performance. This will be discussed in the last section of this chapter.

C. INVERSION OF THE LIDAR EQUATION

The lidar equation can be solved for the volume extinction coefficient, $\sigma(r)$, by substituting Equation (2-3) into Equation (2-1). A convenient form of the received power, $S(r) \equiv \ln (r^2 P(r))$, is now introduced which removes the range dependence from the returned signal and expresses the result in a logarithmic form for analysis purposes [Ref. 12]. The lidar equation can be rewritten, using these definitions and the known $P(r_0)$ from a reference range r_0 (the minimum range for the overlap of the receiver's and transmitter's fields of view):

$$S(r) - S(r_0) = \ln\left(\frac{\beta(r)}{\beta(r_0)}\right) - 2\int_{r_0}^{r} \sigma(r')\, dr' \ . \qquad (2\text{-}4)$$

9

The lidar equation can be further reduced by differentiating both sides with respect to range. The resulting differential equation is as follows:

$$\frac{dS(r)}{dr} = \frac{1}{\beta(r)} \frac{d\beta(r)}{dr} - 2\sigma(r) \ . \qquad (2\text{-}5)$$

The expression for $\beta(r)$, Equation (2-3), can be substituted into Equation (2-5) and results in the following differential equation:

$$\frac{dS(r)}{dr} = \frac{k}{\sigma(r)} \frac{d\sigma(r)}{dr} - 2\sigma(r) \ . \qquad (2\text{-}6)$$

The differential Equation (2-6) is nonlinear because of the k/σ $d\sigma/dr$ term but has the form of a Bernoulli differential equation. It can be shown, by using a linearization transformation ($n = 1/\sigma(r)$), that the resulting solution to the differential equation is:

$$\sigma(r) = \frac{\exp\left[(S(r) - S(r_0))/k\right]}{\dfrac{1}{\sigma(r_0)} - \dfrac{2}{k}\displaystyle\int_{r_0}^{r} \exp\left[(S(r') - S(r_0))/k\right] dr'} \ . \qquad (2\text{-}7)$$

A number of inversion techniques have been used to solve Equation (2-7) [Refs. 11, 13, 14, 15, 16, 17, and 18] and it is not the purpose of this section to describe all of them. One technique, however, has become the standard against which most other techniques are compared; it is the "Klett method" [Ref. 11].

1. Klett Lidar Inversion Method

In the Klett method, instead of integrating Equation (2-7) forward to solve for the extinction coefficient from r to r_0, a boundary value $(\sigma(r_m))$ for the extinction coefficient is determined at the lidar's maximum range (r_m). Then the extinction coefficient can be obtained by integrating backwards from r_m to r. This method has a number of advantages such as the received signal strength being attenuated only to a known value $(P(r_m))$ rather than starting at $P(r_0)$ and decaying. With sensor systems, there will always be a finite limit at which a signal can be detected in noise and the Klett method is better suited to a practical application. The resulting Klett equation is as follows:

$$\sigma(r) = \frac{\exp[(S(r) - S(r_m))/k]}{\frac{1}{\sigma(r_m)} + \frac{2}{k} \int_r^{r_m} \exp[(S(r') - S(r_m))/k] \, dr'} \quad . \tag{2-8}$$

The determination of the extinction coefficient boundary value, $\sigma(r_m)$, becomes very important. The value for $\sigma(r_m)$ can be approximated by relating it to the signal strength $S(r_m)$. Appendix A contains the derivation of this relationship. In summary, the relationship can be obtained through a variable substitution into Equation (2-7), assuming that the average extinction coefficient over the range 0 to r_m is equal to that for r_0 to r_m [Ref. 19] and then substituting the results into the defining expression for S(r). The relationship between $\sigma(r_m)$ and $S(r_m)$ can be expressed as:

$$\frac{S(r_m) - C}{k} + \ln\left(\frac{2(r_m - r_0)}{k}\right) = \ln(\Omega_m) - \frac{r_m}{(r_m - r_0)} \ln(1 + I\,\Omega_m) \quad . \tag{2-9}$$

11

Here the terms C, I and Ω_m are introduced and defined as follows:

1. C is a grouping of lidar constants from the expression for $S(r_m)$ defined as:

$$C = \ln\left(P_o \frac{c\tau}{2} A \text{ Constant}\right) \tag{2-10}$$

2. I is a convenient dimensionless integral term defined as:

$$I = (r_m - r_o)^{-1} \int_{r_o}^{r_m} \exp[(S(r') - S(r_m))/k] \, dr' \tag{2-11}$$

3. Ω_m is also a convenient dimensionless grouping which is related to the expression for I. Ω_m can also be used as a measure of optical depth over the range (r_o, r_m) if the average extinction along the path is equal to $\sigma(r_m)$. Ω_m is defined as:

$$\Omega_m = \frac{2 \, \sigma(r_m) \, (r_m - r_o)}{k} \tag{2-12}$$

A further formal simplification results from setting the left side of Equation (2-9) equal to G_m, which is a constant term. The resulting simplified relationship is then:

$$G_m = \ln\left(\Omega_m\right) - \frac{r_m}{(r_m - r_o)} \ln\left(1 + I\,\Omega_m\right) \tag{2-13}$$

Since G_m is a known quantity, the determination of Ω_m becomes simply an iterative root finding process. In Figure 1 is the graphical representation of the solution curve for Equation (2-13) where the y axis is defined as $\ln(\Omega) - r_m/(r_m - r_o) \ln(1 + I\,\Omega)$. When the solution curve intersects with the value for G_m, a value for $\sigma(r_m)$ can easily be found using Equation (2-12). The selection of the root for Ω_m is ambiguous unless the range and visibility are considered. The solution for the correct root for Ω_m is determined by looking at the limiting cases of high and low visibility conditions and, failing these cases, applying a default algorithm. A summary of the procedure is as follows: [Ref. 20]

12

1. First try the High Visibility algorithm. Using the assumption that the extinction coefficient over the range 0 to r_o is constant, then the value for the integral in Equation (2-1) in this region can be written as $2 \sigma(r_o) r_o$. A new expression for G_m can be obtained by modifying Equation (2-13) for the total path 0 to r_m.

$$G_m' = G_m + 2 \, r_o \, \sigma(r_o) / k = \ln(\Omega_m) - \ln(1 + I \, \Omega_{in}) . \tag{2-14}$$

Equation (2-14) can be rewritten in terms of Ω_m with the resultant form:

$$\Omega_m = \left[\exp(G_m' - I) \right]^{-1} . \tag{2-15}$$

The value of Ω_m is obtained iteratively and its value is assumed correct if $\exp(G'_m) > (I + 0.01)$, if the resulting value for $\sigma(r_m) > 0.01$ and if $\sigma(r_o)/\sigma(r_m) < 50$.

2. If the High Visibility algorithm fails, then try the Low Visibility algorithm. When operating in low visibility conditions, it can be shown that the mean value of the extinction coefficient will depend primarily on the magnitude of the backscattered signal which influences the value for I. A simple approach is used in which the mean of the extinction coefficient is set equal to the boundary value, $\sigma(r_m) (r_m - r_o)$. The resulting equation can be solved iteratively for Ω_m, and $\sigma(r_m)$ determined.

$$\Omega_m = \ln(1 + I \, \Omega_m) . \tag{2-16}$$

The algorithm gives a solution if $I > 1$.

3. If the previous two algorithms fail, then apply the Default algorithm. The default is set to the maximum value for Ω_m when there is no solution to the Klett equation.

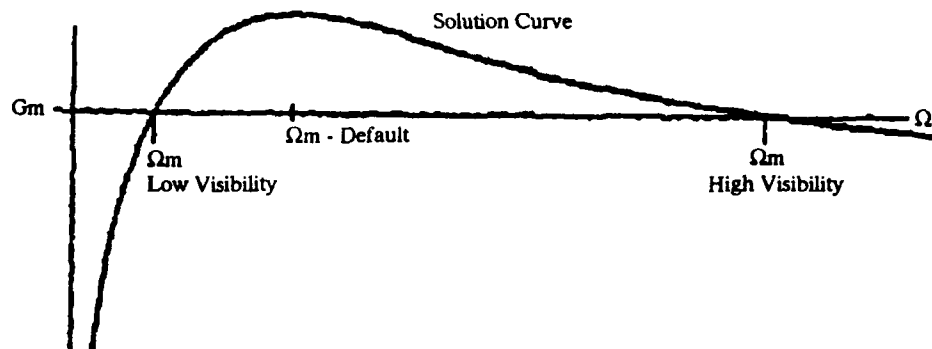$$\Omega_{max} = \frac{(r_m - r_o)}{r_o \, I} . \tag{2-17}$$

Figure 1. Solutions for Ω_m [Ref. 18].

13

A theoretical analysis of lidar returns is conducted in Appendix B using typical extinction coefficient pro....es. The effects of the lidar range resolution and atmospheric noise are considered in the analysis for their effect on the inversion process. The lidar's range resolution is strictly a function of the data sampling rate used to digitize the lidar receiver's analogue signal. The MATLAB high-performance numeric computation software is used for the analysis which produces a S(r) file from a specified path extinction coefficient profile and inverts the S(r) file based on the algorithms outlined above. In some cases, the Low Visibility algorithm was observed to be unreliable, which was also noted by Klett. The simple assumption that the mean of the extinction coefficient is equal to the boundary value, Equation (2-16), is invalid when there is a large dynamic range of the extinction coefficient. The solution for low visibility cases occurs when the G_m line and Ω_m curve are almost parallel and any analysis errors are magnified in the solution.

D. RECEIVER THEORY

The operation and performance of the lidar receiver are as important as the lidar transmitter itself. In this section, the theoretical performance of a photomultipler tube receiver will be studied and characterized. This will lay the ground work for the next chapter concerning system design .

The photomultiplier tube is a vacuum tube photoemissive detector which consists of a cathode, a number of dynodes and an anode as shown in Figure 2. The cathode is a photocathode which generates free electrons when struck by photons of sufficient energy to overcome the cathode work function. The generated electrons are accelerated towards the anode by the electric field between the anode and cathode but are deflected to strike a dynode. The dynodes are electrodes at successively greater potentials and are made up of a material which has a low work function. The free electron collision with the dynode results in the production of several secondary electrons. These electrons are then directed to the

14

next dynode and gains are achieved in the order of 10^6 through successive dynodes and secondary electron production. This gain can be characterized by $G = \delta^N$, where G is the gain, N is the number of dynodes and δ is the number of secondary electrons per impact which is a function of interdynode voltage and dynode material.

The operational use of photomultiplier tubes has been restricted due to:

1. The fragile nature of vacuum devices.

2. The high voltage requirements to achieve sufficient gains (100s of volts per stage).

3. The wavelength restrictions because photocathode spectral response is limited to visible and ultraviolet wavelengths.

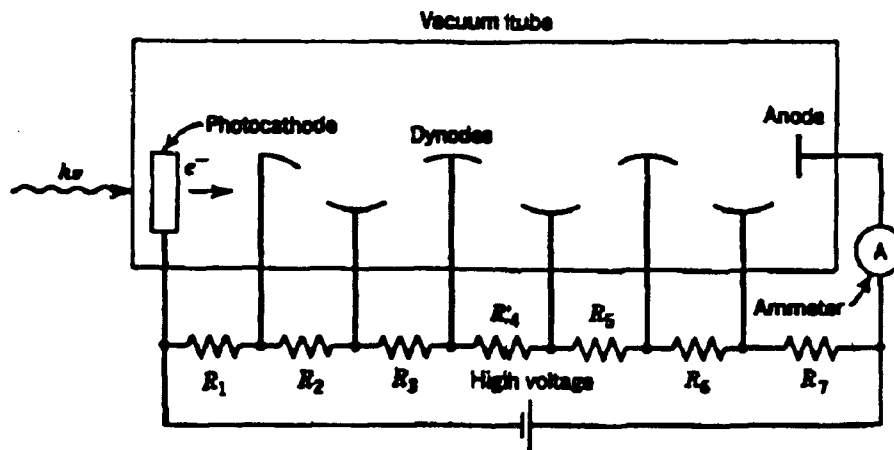4. The low quantum efficiencies, typically 10–25%.

Figure 2. Photomultiplier tube typical layout [Ref. 21].

The photomultiplier tube has continued to be manufactured over the years to meet the needs of the scientific community. Its desirable features are:

1. The high internal gains which allow for the detection of very weak signals.

2. The low internal noise.

3. The fast response times. The typical response times for photomultiplier tubes are in the order of 2 nanoseconds.

The sources of noise in the photomultiplier tube are:

1. Shot noise (i_N). This is noise due the statistical generation process of electrons by the cathode. The rms value of the shot noise current can be written as [Ref. 22]:

$$i_N = \sqrt{2q\left(\overline{i_s} + i_d + \overline{i_b}\right)\Delta f\, G^2}$$ (2-18)

where

$\overline{i_s}$ is the average signal cathode current due to the lidar backscattered photons,
i_d is the dark current (the thermally generated current when no photon flux is
    present at the cathode),
$\overline{i_b}$ is the average cathode current due to the background radiance
    (discussed in the following paragraph),
Δf is the electrical system bandwidth, and
G is the photomultiplier tube gain.

2. Background noise (i_b). This is the shot noise component due the background scene which can be limited by the choice of the receiver field of view and narrowband optical filters. A discussion of this noise source component is felt to be important because it will be the limiting factor for daylight photomultiplier operation. The total generated cathode current is due to the summation of the signal and average background photon flux. These currents are not necessarily independent because the transmitted laser pulse will excite the atomic molecules along the path. The molecular excited state population density is increased with each laser pulse and there is a transition time required to return to the original state. The transition process can be a radiative one, thereby increasing the total background photon flux. In this analysis, this effect will be ignored because it mainly applies to high energy lasers. A general expression for the average background cathode current, assuming no increased background flux, can be written as: [Ref. 22]

$$\overline{i_b} = \frac{\lambda\, q\, \eta(\lambda)\, E_b(\lambda)}{h\, c\, \tau_d}$$ (2-19)

16

where

λ is the wavelength of background radiation,
$\eta(\lambda)$ is the photomultiplier tube quantum efficiency,
$E_b(\lambda)$ is the background spectral energy,
c is the speed of light,
h is Planck's constant, and
τ_d is the detection interval which is different from the laser pulse duration.

The background energy can be written in terms of the receiver's narrowband filter and solid angle assuming that the individual terms which influence the background energy magnitude are constant over the wavelength band interval:

$$E_b(\lambda) = \Delta\lambda\ S_b(\lambda)\ \tau_o(\lambda)\ \Omega_o\ A_o\ \tau_d \qquad (2-20)$$

where

$\Delta\lambda$ is the wavelength interval of the narrowband filter,
$S_b(\lambda)$ is the background spectral radiance (This term can be derived
    from the radiative transfer equation in the visible spectrum where the
    principal scattering mechanism is Rayleigh scattering),
$\tau_o(\lambda)$ is the receiver optics transmittance,
Ω_o is the receiver solid angle,
A_o is the receiver's effective aperture, and
τ_d is the detection interval.

The resultant average background cathode current can be written as follows:

$$\overline{i_b} = \frac{\lambda\ q\ \eta(\lambda)\ \Delta\lambda\ S_b(\lambda)\ \tau_o(\lambda)\ \Omega_o\ A_o}{h\,c} \qquad (2-21)$$

3. Johnson or thermal noise (i_J). This is the noise generated by the thermal excitation of the charge carriers in a resistor. The rms value of the Johnson noise current can be written in the form:

$$i_{J\,rms} = \sqrt{\frac{4\,k\,T\,\Delta f}{R}} \qquad (2-22)$$

where R is the equivalent resistance of the load and photomultiplier tube resistances.

4. Dynode noise. This is the noise due to the statistical fluctuations in the generation of secondary electrons at the dynodes. It can be shown that the noise contribution of the first dynode dominates the noise process of the complete dynode amplification but there is an inverse relationship between the gain of the first dynode and the signal-to-noise-ratio. The dynode noise term can be neglected assuming that the gain of the first dynode is high enough to make the photomultiplier tube gain a noiseless process. [Ref. 21]

The general expression for the power signal-to-noise ratio (SNR) across a load resistor can be written, using Equations (2-19) and (2-22), as follows [Ref. 21]:

$$SNR = \frac{R_{Load} \, G^2 \, i_s^2}{R_{Load} \left(2q \, (\overline{i_s} + i_d + \overline{i_b}) \, \Delta f \, G^2 + \frac{4 \, k \, T \, \Delta f}{R} \right)} \quad . \tag{2-23}$$

A number of limiting conditions can be applied to Equation (2-23). If R is large enough to make the Johnson noise very small compared to the shot noise, then the shot noise will dominate the noise power term and the Johnson noise may be neglected. The remaining two conditions, daylight and nighttime operation, will be discussed in detail because of their importance in determining the maximum range for the lidar system which will become apparent later in the next two subsections.

1. **Daytime Lidar Receiver Operation**

If the photomultiplier tube is used for daylight operation, then the average background current will dominate the dark current and signal current terms for the shot noise term. Therefore, the dark current and signal current terms can be neglected in the analysis. The resultant daylight power SNR from Equation (2-23) will be:

$$SNR = \frac{i_s^2 \, G^2 \, R_{Load}}{2 \, q \, \overline{i_b} \, \Delta f \, G^2 \, R_{Load}} \quad . \tag{2-24}$$

18

The minimum detectable optical power is defined when the signal power across the load resistor is equal to the noise power, or SNR = 1. This value for the SNR is arbitrary but represents the best case scenario for the receiver and also represents the Noise Equivalent Power. An expression for the minimum detectable incident power can be determined by:

1. Noting that the signal current at the cathode can be expressed in terms of the incident power P(r) which is range (time) dependent due to scattering:

$$i_s = \frac{\lambda \, q \, \eta(\lambda) \, P(r)}{h \, c} \quad . \tag{2-25}$$

2. Substituting Equations (2-21) and (2-25) into the expression for the SNR, Equation (1-24).

3. Solving the resultant expression for P(r), with SNR = 1,

$$P(r) = \sqrt{\frac{2 \, h \, c \, \Delta\lambda \, S_b(\lambda) \, \tau_o(\lambda) \, \Omega_o \, A_o \, \Delta f}{\lambda \, \eta(\lambda)}} \quad . \tag{2-26}$$

The maximum range for the lidar system can be approximated by substituting the expression for minimum P(r) (Equation (2-26)) into the general lidar expression (Equation (2-1)) and solving for the range, r. The resulting expression for the maximum daytime range of a photomultiplier lidar system is:

$$r_{max} = \sqrt{\frac{P_o \, \tau \, \beta(r_{max}) \, \sqrt{c \, A_o \, \lambda \, \eta(\lambda)} \, \exp\left[-2 \int_0^{r_{max}} \sigma(r') \, dr'\right]}{\sqrt{8 \, h \, \Delta\lambda \, S_b(\lambda) \, \tau_o(\lambda) \, \Omega_o \, \Delta f}}} \tag{2-27}$$

where

r_{max} is the maximum range for the lidar system (meters),
P_o is the lidar system transmitted power (watts),
τ is the laser pulse duration (seconds),
$\beta(r)$ is the atmospheric volume backscattering coefficient at range r_{max} (meters^{-1} · steradians^{-1}),
c is the speed of light (meters/second),
A_o is the receiver's effective aperture (meter^2),
λ is the wavelength of background radiation which can be approximated as the laser wavelength (meters) because of the narrowband optical filter,
$\eta(\lambda)$ is the photomultiplier tube quantum efficiency,
$\sigma(r)$ is the atmospheric volume extinction coefficient (meters^{-1}),
h is Planck's constant (watts · seconds^2),
$\Delta\lambda$ is the wavelength interval of the narrow band filter (microns),
$S_b(\lambda)$ is the background spectral radiance (watts · meter^{-2} · steradians^{-1} · micron^{-1}),
$\tau_o(\lambda)$ is the receiver optics transmittance,
Ω_o is the receiver solid angle (steradians), and
Δf is the electrical system bandwidth (Hertz).

2. Nighttime Lidar Receiver Operation

For nighttime operation, the signal current (i_s) will dominate the average background current, which can be neglected. The resultant nighttime power SNR from Equation (2-23) will be:

$$SNR = \frac{i_s^2\, G^2\, R_{Load}}{2\, q\, \overline{i_s}\, \Delta f\, G^2\, R_{Load}} \; . \qquad (2\text{-}28)$$

or

$$SNR = \frac{i_s^2}{2\, q\, \overline{i_s}\, \Delta f} \; . \qquad (2\text{-}29)$$

A simplification of Equation (2-29) is possible if the response time of the photomultiplier tube is faster than the laser pulse width used in the lidar transmitter. Then $\overline{i_s}$ over the laser pulse width is approximately equal to i_s. Then Equation (2-29) can be written using Equation (2-25) for the expression for i_s as:

$$SNR = \frac{\lambda \, q \, \eta(\lambda) \, P(r)}{2 \, q \, h \, c \, \Delta f} \, . \qquad (2\text{-}30)$$

An expression for the $P(r)$ can be obtained by setting the minimum detectable optical power across the load resistor equal to the noise power or SNR = 1:

$$P(r) = \frac{2 \, h \, c \, \Delta f}{\lambda \, \eta(\lambda)} \, . \qquad (2\text{-}31)$$

The maximum range for the lidar system can be approximated by substituting the expression for the minimum $P(r)$ (Equation (2-31)) into the general lidar expression (Equation (2-1)) and solving for the range. The receiver optics transmittance ($\tau_o(\lambda)$) must also be taken into account when developing an expression for $P(r)$ and the new expression will be simply Equation (2-31) multiplied by $\tau_o(\lambda)$. The resulting expression for the maximum nighttime range for a photomultiplier lidar system is:

$$r_{max} = \sqrt{\frac{P_o \, \tau \, A_o \, \tau_o(\lambda) \, \lambda \, \eta(\lambda) \, \beta(r) \, \exp\left[-2\int_0^{r_{max}} \sigma(r') \, dr'\right]}{4 \, h \, \Delta f}} \, . \qquad (2\text{-}32)$$

where

  r_{max} is the maximum range for the lidar system (meters),
  P_o is the lidar system transmitted power (watts),
  τ is the laser pulse duration (seconds),
  $\beta(r)$ is the atmospheric volume backscattering coefficient at range r_{max}
      (meters^{-1} · steradians^{-1}),
  c is the speed of light (meters/second),
  A_o is the receiver's effective aperture (meter^2),
  λ is the wavelength of background radiation which can be approximated as the laser
      wavelength (meters) because of the narrowband optical filter,
  $\eta(\lambda)$ is the photomultiplier tube quantum efficiency,
  $\sigma(r)$ is the atmospheric volume extinction coefficient (meters^{-1}),

21

h is Planck's constant (watts · seconds^2),
$\tau_o(\lambda)$ is the receiver optics transmittance,and
Δf is the electrical system bandwidth (Hertz).

The purpose of the derivation of Equations (2-27) and (2-32) is to provide the theoretical basis for the maximum range for a lidar system for day and nighttime operation. In general, the maximum nighttime range will greater than the daylight range because of the background spectral radiance term ($S_b(\lambda)$) present in Equation (2-27) which increases the optical noise in the lidar system and decreases the range.

E. LIDAR WAVELENGTH SELECTION

The selection of the lidar wavelength is an important consideration for the design of any lidar system. In Section B, the atmospheric backscatter coefficient was related to the atmospheric volume extinction coefficient in order to solve the lidar equation; but this relationship was wavelength dependent. The main options for an affordable lidar laser wavelength are in the visible (400–700 nanometers), near-infrared (700 nanometers–2.5 microns) and far-infrared (8–12 microns) regions.

In the visible and near-infrared regions, the relationship between the atmospheric backscatter coefficient and the atmospheric volume extinction coefficient has been shown to be constant over a wide range of size parameters [Ref. 23]. The laser beam divergence for lasers in these regions is small based on the Gaussian far-field full-angle beam divergence formula, 1.27 times laser wavelength divided by twice the beam waist diameter. In theory, a larger photon flux density is possible due to the smaller beam divergence which results in a larger backscattered signal when not taking into account wavelength dependent scattering mechanisms. Therefore, the maximum range of a lidar can be increased by using a laser with a smaller beam divergence. When considering visible and near-infrared lasers for lidar applications, visible lasers will have an advantage based on beam divergence when the laser output energies are the same.

22

There are a number of disadvantages with visible and near-infrared lasers. The main consideration is eye safety. Lasers in the visible and near-infrared regions can be dangerous to the retina of the eye and energy levels must be kept low for external use in urban areas. This restricts the maximum remote sensing range of the lidar. There is also the problem of solar background radiance which can wash out weak lidar signals unless special measures, such as the use of narrowband filters, are taken to reduce the influence of the background in the detector.

In the far-infrared region, there are many advantages. The primary advantage is the issue of eye safety for operation in urban areas. Those lasers operating in the far infrared region are five orders of magnitude safer, based on Maximum Permissible Exposure [Ref. 24], than visible lasers. There are a number of commercial high power lasers in this region which are readily available, such as the carbon dioxide laser (10.6 microns). The carbon dioxide laser has one of the best efficiencies and highest power outputs of commercially available lasers. The solar radiance problem is reduced to the thermal emission of the background which is about one order of magnitude smaller than the visible region background radiance [Ref. 22].

As with visible and near-infrared lasers, the far-infrared laser has a number of disadvantages. In this region, the relationship between the atmospheric volume backscatter and atmospheric volume extinction coefficient is not as linear as in the visible region. The magnitude of the backscatter coefficient in the far infrared is almost two orders of magnitude smaller than a corresponding visible region value [Ref. 25]. The result for far-infrared lasers is a one hundred fold increase in the pulsed energy output required to achieve the same lidar performance as a visible laser (using Equation (2-1)), but commercially available carbon dioxide lasers can provide the needed energy levels. The final disadvantage of lidar operation in this region is beam divergence which is

approximately 100 times worse than in the visible region and will limit the maximum operating range.

The choice of a lidar system wavelength is not an easy one and is dependent on the employment and measurements to be made. In this thesis, a frequency-doubled Nd:YAG laser was used (532 nanometers) mainly due to availability as well as its many advantages over far-infrared lasers as discussed above.

The next chapter will deal with the actual design, manufacture and calibration of a frequency-doubled Nd:YAG lidar system.

III. LIDAR SYSTEM DESIGN

A. OVERALL DESIGN

The design of the lidar system was carried out for the maximum possible range subject to the constraints of laser availability and eye safety. The designed system consists of a frequency-doubled Nd:YAG medical laser, a 17.75 inch telescope for the transmitting optics, a photomultiplier tube with associated optics used as the detector, a digital oscilloscope for data collection and display and a computer for data acquisition, storage and off-line processing. A schematic of the overall lidar design is featured in Figure 5. The main constraint for the design of the lidar was laser safety since the lidar will be used for atmospheric studies and will be located on the school grounds.

The initial lidar design was based on a large area Fresnel lens, but in testing it was found to be unsuitable for beam expansion. The Fresnel lens used was an Edmund Scientific experimental Fresnel lens D34,747 which was approximately 28 inches by 37 inches and had a focal length of 54 inches [Ref. 26]. The 40 lines per inch on the lens was not sufficiently high enough to produce a good quality collimated beam. This lidar design could not progress further until an alternative beam expander was found. A search of the NPS Physics Department revealed an old telescope which was used in the final design.

B. LIDAR TRANSMITTER

1. Laser

The laser used in the lidar transmitter was a Nd:YAG laser model MK 100 manufactured by Kigre Incorporated. The laser was later modified by Kigre Incorporated with an extra-cavity frequency-doubling crystal to provide a 532 nanometer wavelength output. The system consisted of a laser head and separate power supply. The power supply incorporates a control unit which allows the selection of the number of pulses per

Laser and associated optics

Nd:YAG 532
nanometers

17.75"
Dall-Kirkham
telescope

PMT

Tektronix
DSA 602A
Digital
Oscilloscope

Detector with
photomultiplier tube

Floppy Disc
Data Transfer
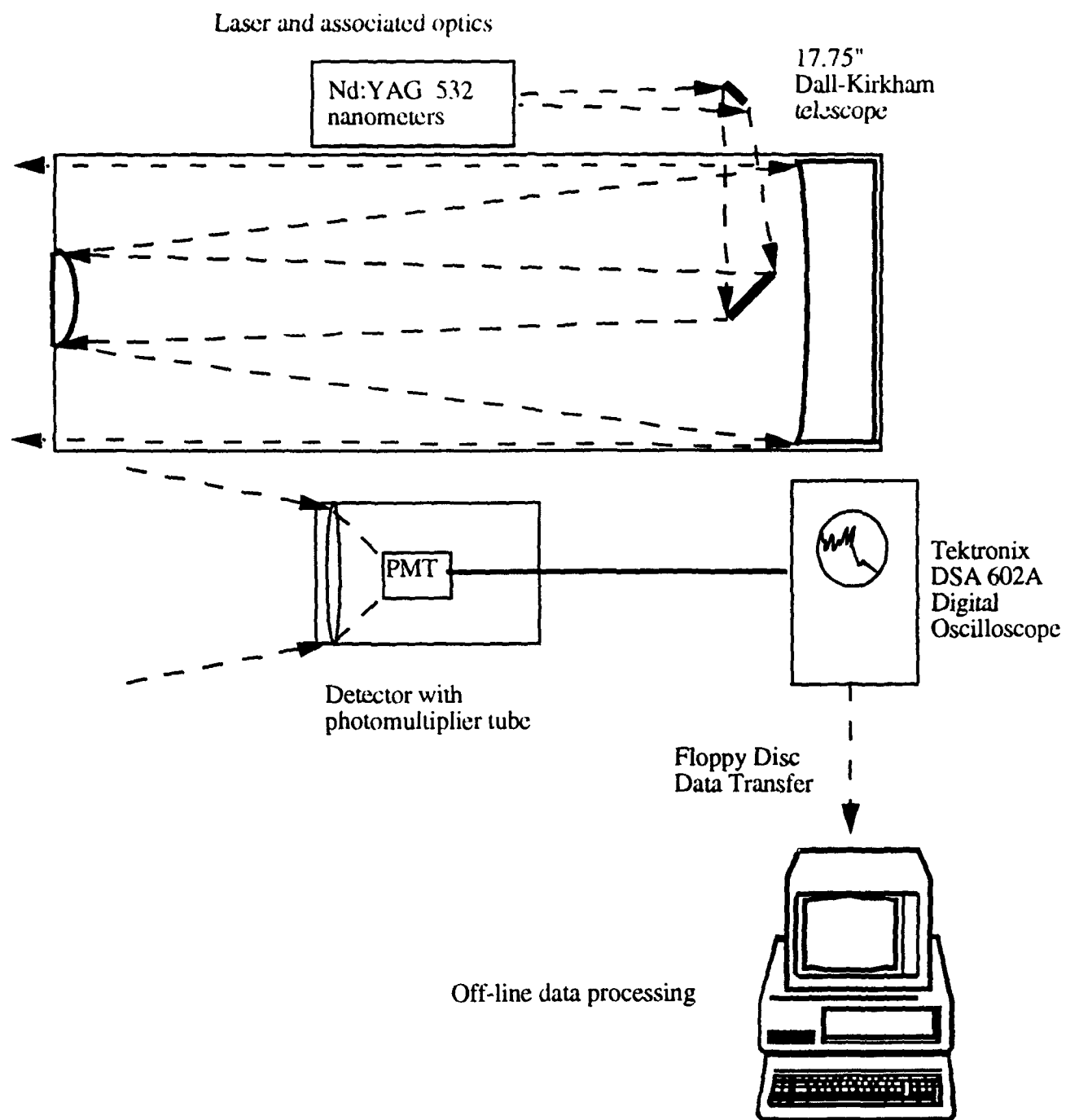
Off-line data processing

Figure 5. Lidar System Schematic.

firing (1–5), the energy per pulse and a laser energy monitor display. A summary of the laser's specifications is in Table 1.

After the frequency-doubling process, both the original 1.06 micron and the frequency-doubled 532 nanometer wavelengths were present in the laser output. As discussed in Chapter 2, the visible wavelength was desired due the strong relationship between $\sigma(r)$ and $\beta(r)$. Therefore, it was necessary to remove the 1.06 micron beam from the main laser beam. It was noted that the laser's energy density was not the classic Gaussian profile as expected and there was an off-axis laser artifact present with enough energy to produce a burn mark in carbon paper, as shown in Figure 6. The discovery of the artifact was important as it required removal for laser safety reasons. The Nd:YAG laser's external optics were inspected by the author and nothing was found which could suggest the cause of the laser beam energy profile. It was therefore assumed to be a possible misalignment of the frequency-doubling crystal which was sealed. The only option to correct this problem was to return the laser to Kigre Incorporated for repair, but this would have imposed unacceptable delays in the completion of the thesis. It was therefore decided to complete the thesis and investigate the possibilities for the Nd:YAG laser repair at a later date.

It was observed, after a large number of laser firings, that the energy output of the Nd:YAG laser varied from shot to shot from those measured in Table 1. This should not present a problem, since only the maximum energy values will be used in any laser safety calculations.

TABLE 1. Nd:YAG LASER SPECIFICATIONS [Ref. 27]

Characteristic	Value	Comment
Maximum Energy Output (5 pulses per shot)	mean = 9.126 millijoules σ = 1.587 millijoules	Provided by Kigre Incorporated for a 532 nanometer 100 shot test.
Beam Diameter	4.0 ± 0.2 millimeters	Determined by experimentation using laser burn marks.
Half Angle Beam Divergence	0.165 ± 0.001 milliradians	As above.
Energies Available (Single shot only)	Laser Setting Measured Values 0.15 0.14 0.25 0.34 1.0 0.43 2.5 0.74 4.0 1.04 5.0 1.96 7.5 2.44 10.0 2.09 All values listed in millijoules.	Determined experimentally for 532 nanometers using a 1.06 micron laser safety filter.

28

4 mm

High
energy →
area

Lower
energy
area

1.25 mm

Off-axis artifact approximately 1 mm in
diameter
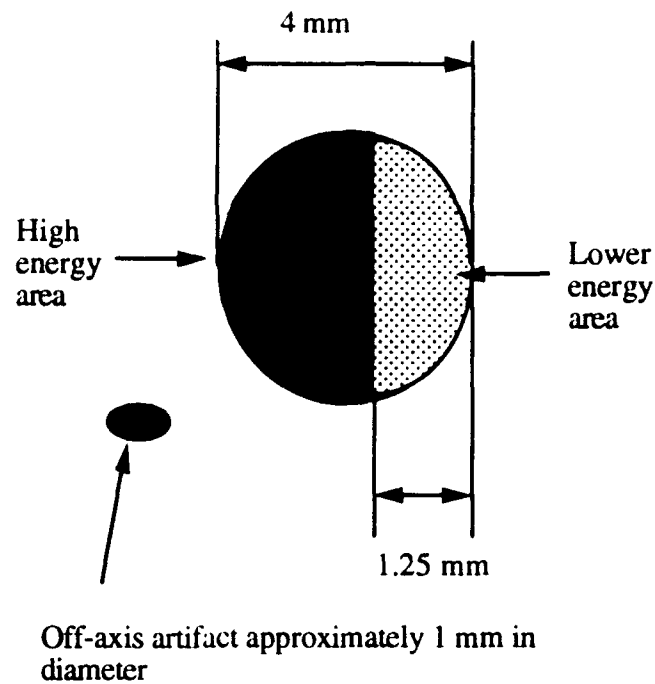
Figure 6. Nd:YAG Laser Beam profile.

2. Dall-Kirkham Telescope

The Dall-Kirkham telescope is a form of Cassegrain telescope but the primary
mirror is aspheric and the secondary is spherical. A summary of the telescope's
specifications is in Table 2.

The telescope was used initially for atmospheric studies in the 1970s and it was
refurbished for use in this lidar application. The original mirror smoothness was quoted as
a tenth of a wavelength at 632.8 nanometers but an inspection of the mirrors found a
number of pits in the coating. It is probable that the smoothness is no longer to this
precision due to salt corrosion; but for this lidar application the existing mirror quality will
be more than adequate since the telescope is not being used for imaging. Also any

29

additional mirror losses due to the corrosion can be made up easily by increasing the laser output energy. The telescope has a 4 inch diagonal to redirect the focal plane 90 degrees to the telescope axis and it will be also used for the lidar application.

TABLE 2. DALL-KIRKHAM TELESCOPE SPECIFICATIONS [Ref. 28]

Manufacturer	Tinsley Laboratories Incorporated 3900 Lakeside Avenue Richmond, California 94806 In approximately early 1970s
Primary Mirror	Diameter - 17.75 inches (aspheric) Radius of Curvature - 126 inches Focal length - 63.0 inches Optical coating - Al/SiO Substrate - Cervit F number - 3.55
Secondary Mirror	Diameter - 5.75 inches (spherical) Radius of Curvature - 44.80 inches Optical coating - Al/SiO Substrate - Cervit

Overall System	Effective focal length - 252 inches
	Mirror separation - 46.25 inches
	    (vertex to vertex)
	Effective F number - 15.0
	Focal plane is 21.0 inches behind vertex of
	    primary mirror.

The telescope was mounted on a Pelco PT2000L Pan and Tilt Unit to have the ability to align the lidar on targets of interest. The unit has a $\pm 90°$ adjustable tilt and 355° adjustable pan movement [Ref. 29]. A camera and surplus right-angle telescope were

available for mounting on to the telescope to provide an indication of the telescope's field of view as well as a warning of obstructions but time did not permit their installation.

3. Laser Optics

The lidar transmitter laser optics layout is shown at Figure 7. The 1.06 micron wavelength beam was split from the 532 nanometer main laser beam and directed into a beam stop using a 1.06 micron reflecting beam splitter. The provision was made for future use of the 1.06 micron wavelength, if required, by the addition of infrared optics. The choice of the beam expanding optics was very important in order to properly fill the telescope's secondary mirror without loss of energy. In the calculations for the beam expander optics, it was decided to transmit as much laser energy as possible into the atmosphere. Therefore, the 99% beam radius point was taken as pi times beam waist divided by two (or 3.141 millimeters). The radius of the secondary mirror was chosen as the 99% point and the distance to focal point was used in the calculations. The matrix representation for the solution using only one lens is shown below:

$$
\begin{bmatrix} w' \\ \theta' \end{bmatrix} = \begin{bmatrix} 1 & T \\ 0 & 1 \end{bmatrix} \begin{bmatrix} 1 & 0 \\ \frac{-1}{f} & 1 \end{bmatrix} \begin{bmatrix} w_0 \\ \theta_0 \end{bmatrix}
\tag{3-1}
$$

where

w' is the beam radius on the secondary mirror at the $1/e$ point (46.49 millimeters),
θ' is the beam half angle beam divergence needed to fill the secondary at the $1/e$ point and knowing the focal plane location (27.229 milliradians),
T is the distance from the secondary mirror to lens,
f is the focal length of lens.
w_0 is the measured laser beam waist (radius 2.0 millimeters), and
θ_0 is the measured laser half angle beam divergence (0.165 milliradians).

31
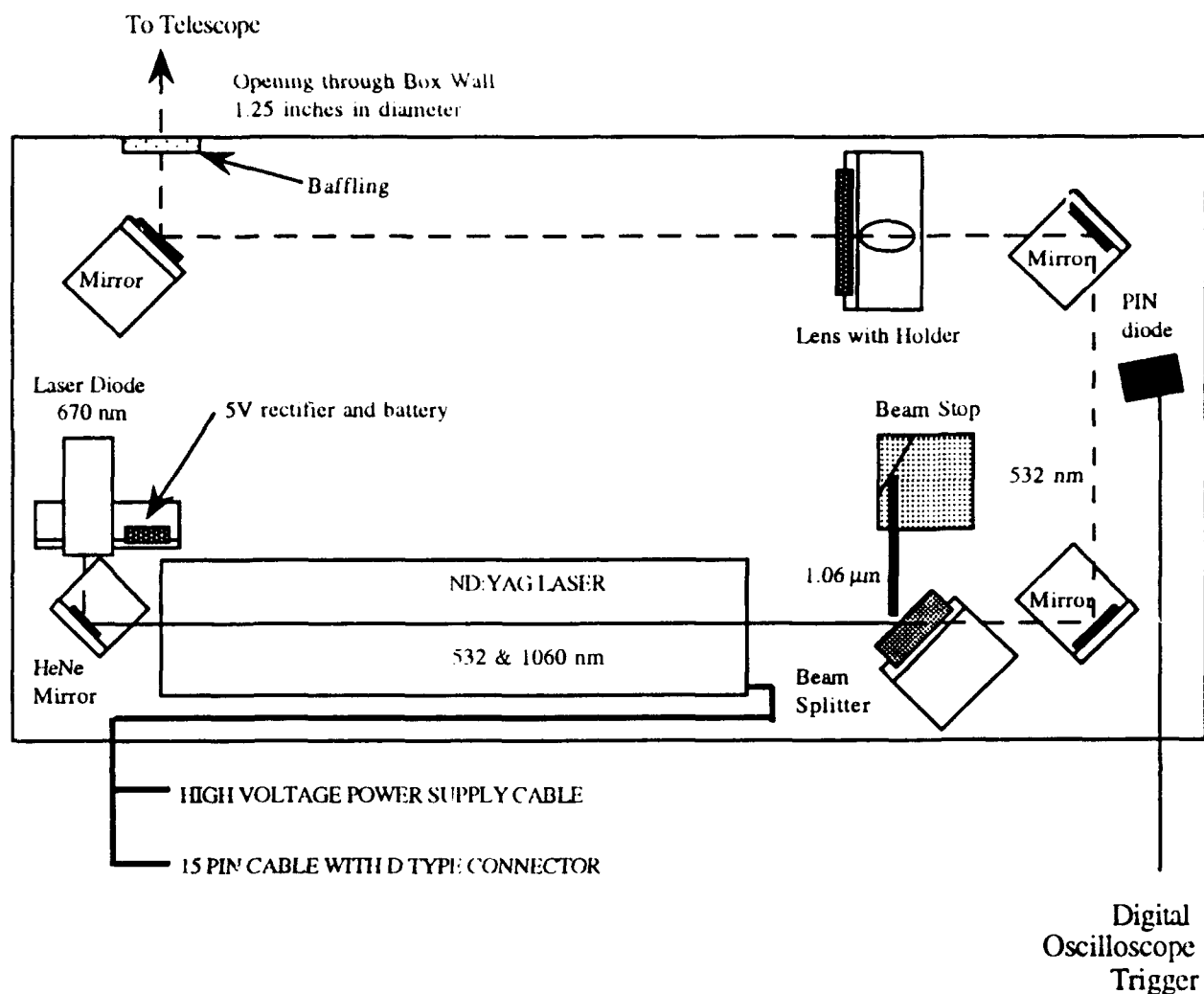
Figure 7. Laser Box Optics.

The lenses used in the beam expander were restricted to those readily available within the NPS Department of Physics. A -74 millimeter focal length meniscus lens was determined to be the best design to expand the laser beam from Equation (3-1). The distance for the lens from the secondary mirror was determined to be 163.4 centimeters using Equation (3-1). Other designs using multiple lenses were considered but disregarded as showing no advantage over the simpler single lens approach.

32

The Nd:YAG laser had the capability to incorporate a helium neon laser as a pointing device; this capability consisted of a electrical power connection and the front and rear Nd:YAG mirrors were transmissive at 632.8 nanometers. The helium neon laser was not purchased with the Nd:YAG laser, so a visible 670 nanometer red laser diode was substituted. The laser diode was used as a diagnostic tool for the alignment of the Nd:YAG laser beam in the laser box without constantly firing the Nd:YAG laser. A 9 volt battery was used to power the laser diode in order to have an independent power supply. The 9 volt power supply, without the battery, was left inside the sealed laser box for future beam alignment. There was a concern about damage to the laser diode due to the 1.06 micron laser beam energy leakage from the Nd:YAG rear mirror, which was measured at a constant 0.25 millijoules for all single pulse shot settings. A helium neon laser mirror, transmissive at 1.06 microns, was placed directly behind the rear mirror of the Nd:YAG laser, as shown in Figure 7, to prevent the 1.06 micron laser beam energy leakage from damaging the laser diode.

A surplus PIN photodiode was added into the design in order to trigger the digital oscilloscope for lidar backscatter measurements. The PIN photodiode was placed inside the laser box and it was aimed at one of the mirrors. There was enough energy scattered from the mirrors for the PIN diode to produce a signal which would trigger the oscilloscope. The Nd:YAG flash lamp was observed at the PIN photodiode output and a highpass filter was built using a floating ground to isolate the Nd:YAG laser pulses. The floating ground was required because the very large current surge from the flash lamp caused an induced surge in the common ground. The PIN photodiode and associated highpass filter were then used to trigger the digital oscilloscope to start the lidar measurements.

After initial testing of the laser box mounted with the telescope, an overfilling of the secondary mirror was observed which in the far-field appeared as an expanding ring encircling the collimated lidar beam. This overfilling was attributed to a slight misalignment of the beam expanding lens (which was later corrected) and the non-Gaussian laser beam shape causing the laser beam edges to be of a higher energy density than expected. It was decided to employ a baffle, or iris, to restrict the exit aperture out of the laser box to that needed to fill the secondary mirror.

The half-angle beam divergence for the lidar transmitter was determined to be 0.794 milliradians by measuring the growth of the laser beam's diameter over a known distance. The beam divergence was decided to be adequate for lidar use and safety considerations, since the laser beam would never focus in the far-field.

C. LASER SAFETY

Laser safety was an important consideration in the design of the lidar. In the designed configuration, the laser beam must be greatly expanded using a telescope in order to achieve a maximum allowed energy density, the Maximum Permissible Exposure (MPE), of 5×10^{-7} joules per centimeter^2 [Ref. 24]. The energy density of the transmitted laser beam was measured using a Laser Precision Corporation energy meter which had a 200 microjoule range and a five square centimeter detection area. Since the secondary mirror blocked the transmission of the peak laser energy along the optical axis, the peak transmitted energy density was found along the edge of the secondary mirror as expected. The measured peak energy densities in the expanded laser beam for different laser setting is shown in Table 3.

The range along the unobstructed optical axis of the laser beam, which it can be safely viewed by the human eye, is referred to as the Nominal Ocular Hazard Distance (NOHD) [Ref. 24]. The NOHD defines the range at which the wavelength specific MPE is

34

not exceeded. This distance is one of the principle measures of laser eye safety and it will be determined for each laser setting. The NOHD can be calculated from the average radiant exposure, Equation B9 in reference 24, which is defined as the energy of the laser beam divided by its total area:

$$H = \frac{Q \exp[-\mu r]}{\pi \left[\frac{(a + r\, \phi)}{2}\right]^2}$$ (3-3)

where

H is the radiant exposure measured in joules per centimeter^2,
Q is the radiant energy output of a pulsed laser measured in joules
    (defined at the 1/e points of maximum irradiance),
μ is the atmospheric extinction coefficient,
r is the range in centimeters,
a is the laser beam diameter measured to 1/e points in centimeters, and
ϕ is the laser beam divergence
    (twice the half-angle beam divergence, 1.588 milliradians).

In the case of this application, the lidar has a secondary mirror which blocks the center transmission of laser beam, as shown in Figure 5. The total radiant energy output, Q, which actually exits the lidar transmitter, can be determined from the fraction of the total power which is blocked by the secondary mirror and noting that Q is equal to total power divided by laser pulse duration. The fraction of the total power or energy of a Gaussian beam, which is blocked by the secondary mirror, is obtained using the following relation:

$$\frac{P_d}{P_o} = 1 - \exp\left(\frac{-2\, D_o^2}{D_L^2}\right) = 0.4045$$ (3-4)

where

P_d is the power blocked by the secondary mirror,
P_o is the total power of the laser beam,
D_o is the diameter of the secondary mirror (14.61 centimeters), and
D_L is the laser beam diameter measured from the 1/e points
       (28.7 centimeters - twice the diameter of telescope divided by π,
       since the telescope was designed to transmit 99% of the laser energy).

The denominator of Equation (3-3) must also be modified to account for the reduction of laser beam area due to the blocking of the secondary mirror. The modified laser beam area can be simply written, using previously defined terms, as:

$$\pi \left[\frac{(a + r \phi)}{2} \right]^2 = \pi \left[\frac{(D_L + r \phi)}{2} \right]^2 - \pi \left[\frac{D_o}{2} \right]^2 . \tag{3-5}$$

An expression for the lidar radiant exposure, H, can be written by substituting Equation (3-5), and the value from Equation (3-4) into Equation (3-3). Q can be written in terms of the total laser beam energy by noting that 86% of the laser's energy is found between the 1/e points of maximum irradiance; Q = 0.86 times the total laser beam energy. The resulting new expression for H is:

$$H = \frac{(1 - 0.4045) \, 0.86 \, Q_T \exp\left[-\mu r\right]}{\pi \left[\frac{(D_L + r \phi)}{2} \right]^2 - \pi \left[\frac{D_o}{2} \right]^2} . \tag{3-6}$$

where Q_T is the total energy of the laser beam.

TABLE 3. LASER SAFETY

Laser Setting	Total Laser Energy Measured at Laser Box Exit - 5 shot average (see text). Q_T (millijoules)	Peak Energy Density Measured using 5 cm² Energy Probe across Telescope. (microjoules per cm²)	NOHD (meters) Worst Case - no atmospheric attenuation. (see text)
10	2.414	2.0	184.1
7.5	2.06	2.96	158.1
5.0	1.96	1.58	150.4
4.0	1.123	1.34	77
2.5	1.7	1.125	129.7
1.8	1.885	0.6725	144.5
1.2	1.61	0.352 (see text)	121.9
0.9	0.917	0.352 (see text)	55.5

A worst case estimate for the NOHD can be obtained from Equation (3-6) if the atmospheric extinction coefficient term is neglected, exp [-μr], and H is set to the MPE. The resulting first order differential equation, in terms of the range, can be solved for each total laser energy output as shown in Table 3:

$$r^2 + \frac{2D_L}{\phi} r + \frac{(D_L^2 - D_o^2)}{\phi^2} - \frac{(1 - 0.4045)\, 0.86\, Q_T}{\frac{\pi}{4} MPE} = 0 \; . \qquad (3\text{-}7)$$

Upon closer inspection of Table 3, there were observed a number of inconsistencies in the measured energy densities for laser settings 0.9 and 1.2 and the calculated NOHD. The values for the NOHD should have been very small based on the MPE, but they were not. A more realistic indication of laser safety would the peak energy density measured across the telescope as shown in the third column of Table 3.

It was noted that the measured laser box energy values, shown in the second column of Table 3, were different from those measured in Table 1. This could be attributed to possible misalignment of the neutral density filters which are mounted in the Nd:YAG laser and provide the selectable energy settings. This problem could not be repaired by the author.

D. LIDAR RECEIVER

The designed lidar receiver layout is at Figure 8. The receiver was designed to have a larger field of view than the transmitter to ensure that as much of the backscattered photon flux as possible would be collected. The receiver's collecting lens had a focal length 250 millimeters and had a diameter of 145 millimeters.

There were two techniques employed for reducing the amount of background sky radiance collected by the receiver, a pin-hole and a narrowband filter. An one-eighth inch diameter pin-hole was placed in the focal plane of the receiver's collecting lens. The resulting reduced field of view was calculated to be 0.127×10^{-3} steradians or a half angle subtense of 6.35 milliradians. A smaller pin-hole could be used to improve the far-field lidar signal by reducing the background in the field of view and thereby improving the SNR. A ten-nanometer narrowband optical filter centered at 532 nanometers was also used in the lidar receiver, which reduced the overall background radiance to a very narrow band

around the laser wavelength. A collimating lens was positioned in front of the narrowband filter to ensure that all of the collected photons passing through the pin-hole would strike the photocathode and not miss it due to divergence.

The photomultiplier tube used was a Hamamatsu R1913. It was chosen for its fast rise response time and its sensitivity in the visible region. The specifications of the R1913 photomultiplier tube are in Table 4.
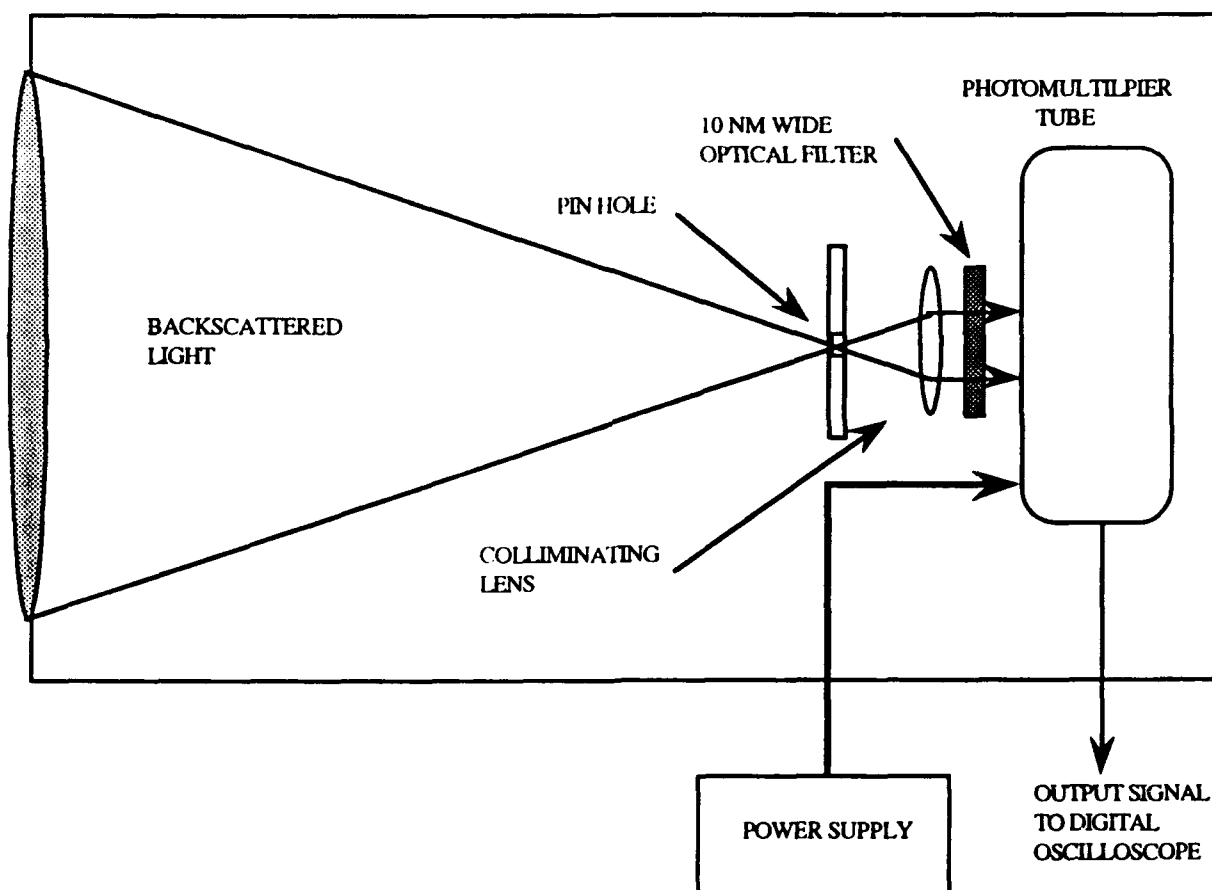

Figure 8. Lidar Receiver.

The output of the photomultiplier tube was to be amplified using a Model VV100B wideband pulse amplifier made by the LeCroy Corporation in the initial design of the lidar

receiver. The amplifier has a gain of 10, less than 2 nanosecond rise time and > 200 megaHertz bandwidth [Ref. 30]. The LeCroy Corporation also makes a mounted version of the Model VV100B (which has the designation Model VV100BTB) and it had the proper ground planes and components for low noise operation which made it ideal as a lidar signal amplifier. The amplifier was not required in the final design because the digital oscilloscope used to acquire the data was very sensitive; also there was a lot of noise in the lidar system. The source of the electrical noise was not found and it was decided that the amplifier would only compound the problem by amplifying the noise. The amplifier is planned for use in a modified design of this lidar where photon counting lidar techniques are to be used after the noise source is eliminated.

TABLE 4. R1913 PHOTOMULTIPLIER SPECIFICATIONS [Refs. 31 and 32]

Cathode Sensitivity	65 milliAmperes per Watt (typical) 55 milliAmperes per Watt (532 nanometers)
Current Gain	3.0×10^3
Response Time	1.0 nanoseconds (at 2000 VDC)
Anode Dark Current	Typical 0.05 nanoAmperes Maximum 0.5 nanoAmperes
Spectral Response	Range 185–900 nanometers Peak Wavelength 420 nanometers
Quantum Efficiency	Average in the Visible Region 13% At 532 nanometers 15 %

40

E. LIDAR ALIGNMENT

1. Telescope

The telescope was collimated for the lidar application, employing an amateur astronomer technique [Ref. 33] without the 4 inch diagonal mirror, using a sufficiently bright star in the Monterey Bay sky to obtain an observable focused point of light at the focal plane. The focal plane was then adjusted by moving the secondary mirror so that the focal plane was 21.0 inches behind the vertex of the primary mirror as given in the telescope's specifications. The mechanical alignment of all the mirrors was accomplished by observing the double reflection from the secondary and primary mirrors of the author's eye centered in the diagonal mirror .

The confirmation of the collimation was done by using a second smaller telescope, which was focused at infinity. A light source was placed in the large telescope's focal plane and then the smaller telescope was placed in the large telescope's field of view. The theory for this method of collimation was that if the light source was at the focal plane of the large telescope, then the image of the light formed by the smaller telescope would be in focus, and it was.

2. Lidar Transmitter and Receiver Alignment

The lidar transmitter was initially aligned using the red laser diode shown in Figure 7. In theory, if the red laser diode was aligned with the Nd:YAG laser, the mirrors could be adjusted so that the unexpanded red laser diode reflection off the secondary mirror followed its path back into the laser box. Then, the Nd:YAG laser axis was aligned to the telescope's secondary mirror axis. In practice, the alignment of the red laser diode to the Nd:YAG laser axis was never really achieved because of problems with precisely mounting the laser diode. The laser diode was able to provide a reasonably accurate pointing for the Nd:YAG laser and this was used to roughly align the Nd:YAG optical axis with the

41

telescope's optical axis. A more precise alignment was conducted by measuring the energy density distribution around the secondary mirror obstruction. If the lidar transmitter was aligned, then the energy density would follow the energy pattern in Figure 6. A baffle was used to restrict the size of the expanded Nd:YAG laser beam as mentioned in Section B. The telescope's secondary mirror was slightly adjusted to compensate for any inaccuracies in the laser box alignment. The telescope's primary mirror was never adjusted. The beam shape and energy distribution of the collimated laser beam was observed by using a locally made cardboard screen painted florescent yellow. The yellow florescence after irradiation by the laser beam was easily observed through the laser safety goggles and this was a very inexpensive method to view the beam.

The lidar receiver was aligned after the lidar transmitter alignment. It was accomplished by adjusting the position of the receiver pin-hole to obtain the largest returned signal from the painted cardboard screen in the laboratory. The procedure was again repeated once the lidar was installed on the roof of Spanagel Hall using the same painted cardboard screen but at a longer distance.

F. DATA ACQUISITION

The measurement and digitizing of the backscattered lidar signal was accomplished using a Tektronix DSA 602A Digitizing Signal Analyzer which had a two gigasample per second sampling rate [Ref. 34]. A signal bandwidth of 1 gigaHertz was obtained by using an 11A72 two-channel plug-in module. The Tektronix DSA 602A had a MS-DOS 3.5 inch disc drive built into it which was a useful feature. This allowed data storage directly to disc, otherwise the data would have to be transferred to a computer and then to disc which would be a slower process. The range resolution for DSA 602A was calculated to be 0.15 meters but this is the two-way range resolution and needs to be divided by two to reflect the

42

range at which the backscattered signal originates. The actual timebase range resolution is dominated by the laser pulse width (τ) and is estimated as 0.6 meters ($c\tau/2$).

The Tektronix DSA 602A became available at the last minute, but, initially it was planned to use the Hewlett Packard HP54111D Digitizing Oscilloscope which had a sampling rate of 1 gigasample per second. In order to store the data for off-line analysis using the Hewlett Packard HP54111D, a computer interface was required as described in the previous paragraph. The Tektronix DSA 602A was chosen over the Hewlett Packard HP54111D mainly because of the ease of data storage. The theoretical lidar inversion analysis conducted, in Appendix B, used the Hewlett Packard HP54111D sampling rate which provided a one-way timebase range resolution for the lidar inversion of 0.15 meters. It was decided not to change the analysis to reflect the new range resolution since the small change would not have produced any better results.

The lidar backscattered signal could have been observed more easily if a logarithmic amplifier was used at the oscilloscope input. The logarithmic amplifier would expand the lidar backscattered display by amplifying the far-field return while leaving the near-field return in its original form. This would allow both the near- and far-field returns to be observed. The data could be reverted to its original form by using the manufacturer's logarithmic amplifier specifications. This would be a possible future design modification.

The next chapter will present various actual measured lidar signals from hard targets and clouds.

IV. LIDAR DEMONSTRATION AND RESULTS

A. DEMONSTRATION OVERVIEW

On 9 June 1993 at 1945 hours, the lidar designed in Chapter III was tested to ensure that it could provide range data to clouds which was the primary aim of this thesis. The weather conditions were clear with light clouds and fog over Monterey Bay. There was a fog bank forming off the coast, and later in the evening it was ranged to. The lidar was operated under strict control of the NPS Physics Department staff and the author was present to take data. The data was recorded using the Tektronix DSA 602A Digitizing Signal Analyzer as described in Chapter III. Both the lidar receiver and transmitter trigger signals were stored by the oscilloscope and the trigger signal was used in the later analysis to confirm the start time for the lidar return. The aim of the demonstration was to obtain a range to hard targets initially and then to clouds.

B. RANGE RESULTS

The lidar was initially tested against hard targets to determine if a reflected signal could be observed by the lidar receiver. A tree on the school grounds was used as the first hard target, estimated at about 300 meters from the lidar. The lidar transmitter range domain signal is displayed in Figure 9 for the tree target. The tree return is clearly visible in Figure 9 and this confirmed the lidar's ranging ability for short ranges. The digital oscilloscope was not used in its highest resolution because this was a proof of concept demonstration only vice actual atmospheric studies. Ranges were also obtained to the Jacks Peak Ridge which runs southwest of the city of Monterey. The range measured from a city of Monterey map indicate the range from the school to the ridge to be in the order of five kilometers. The ranges observed were approximately six kilometers which are considered more accurate.
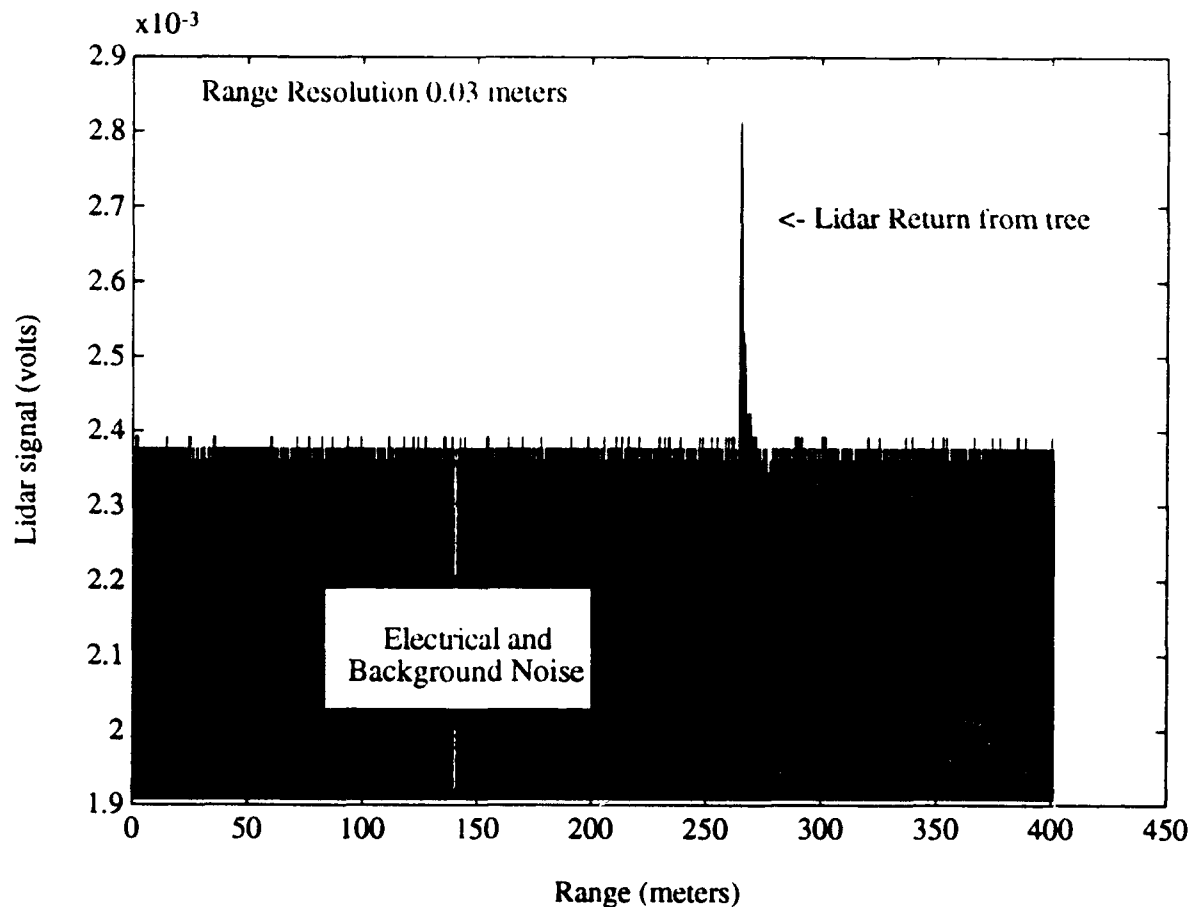
Figure 9. Lidar return from tree on campus grounds at approximately 2015 hours.

The next demonstration of the lidar was the ranging to clouds. During the course of the evening, a number of light cumulus clouds began to blow in from the ocean and they were successfully ranged. Figure 10 is an example of one such cloud ranging. This figure also has some interesting features such as the characteristic near-field exponential decay of the lidar signal as it propagates away from the lidar receiver and a strong cloud lidar signal. The cloud was visually estimated to be one kilometer and the actual range determined from Figure 10 was 1400 meters. The lidar was able to successfully range to clouds with good agreement from visual estimation. A number of other clouds were ranged during the

course of the evening and a variety of lidar returns were observed. There were variations in the magnitudes of the lidar cloud returns which were attributed to the changing nature of the atmosphere due to a strong breeze blowing in from the ocean.
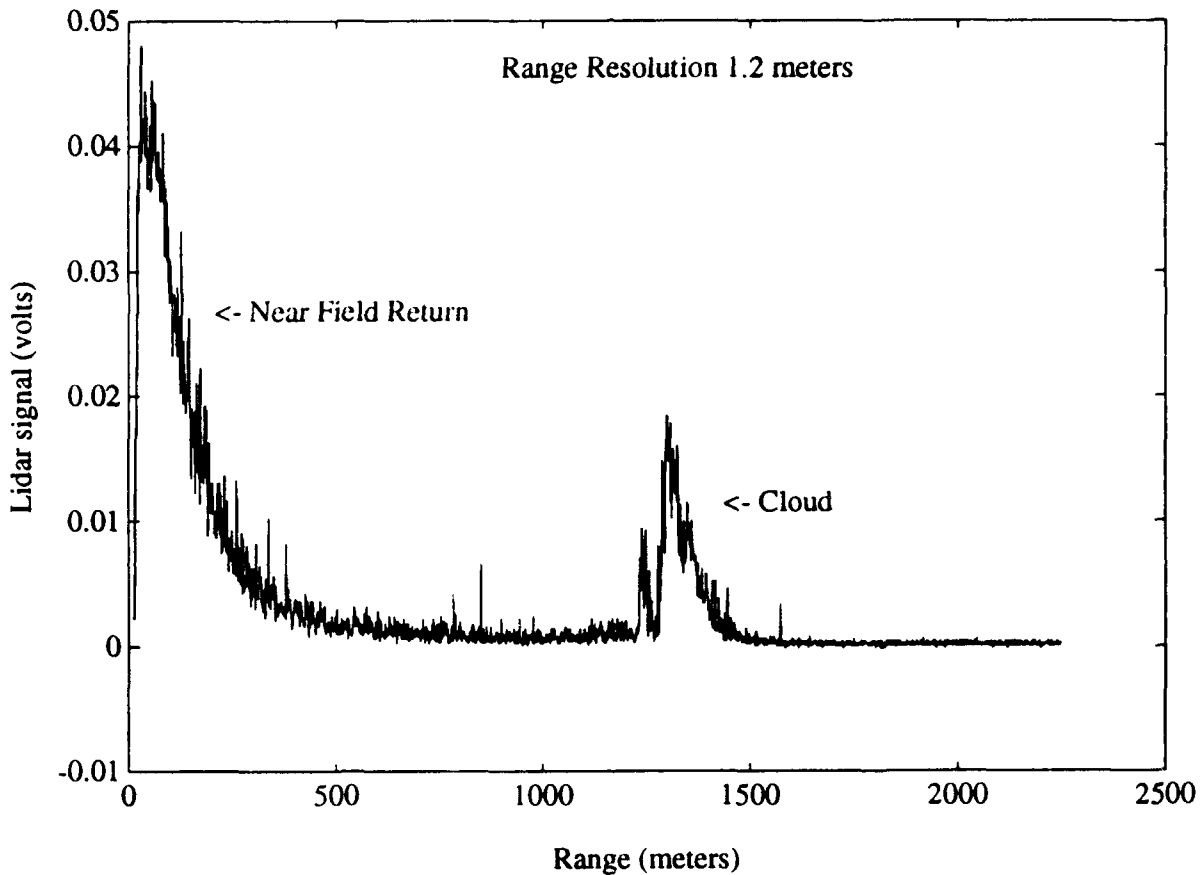

Figure 10. Lidar return from a cloud at approximately 2040 hours.

The last lidar measurements, taken at approximately 2110 hours, were of the fog bank off the coast which was observed forming earlier. The fog bank lidar return is shown in Figure 11.
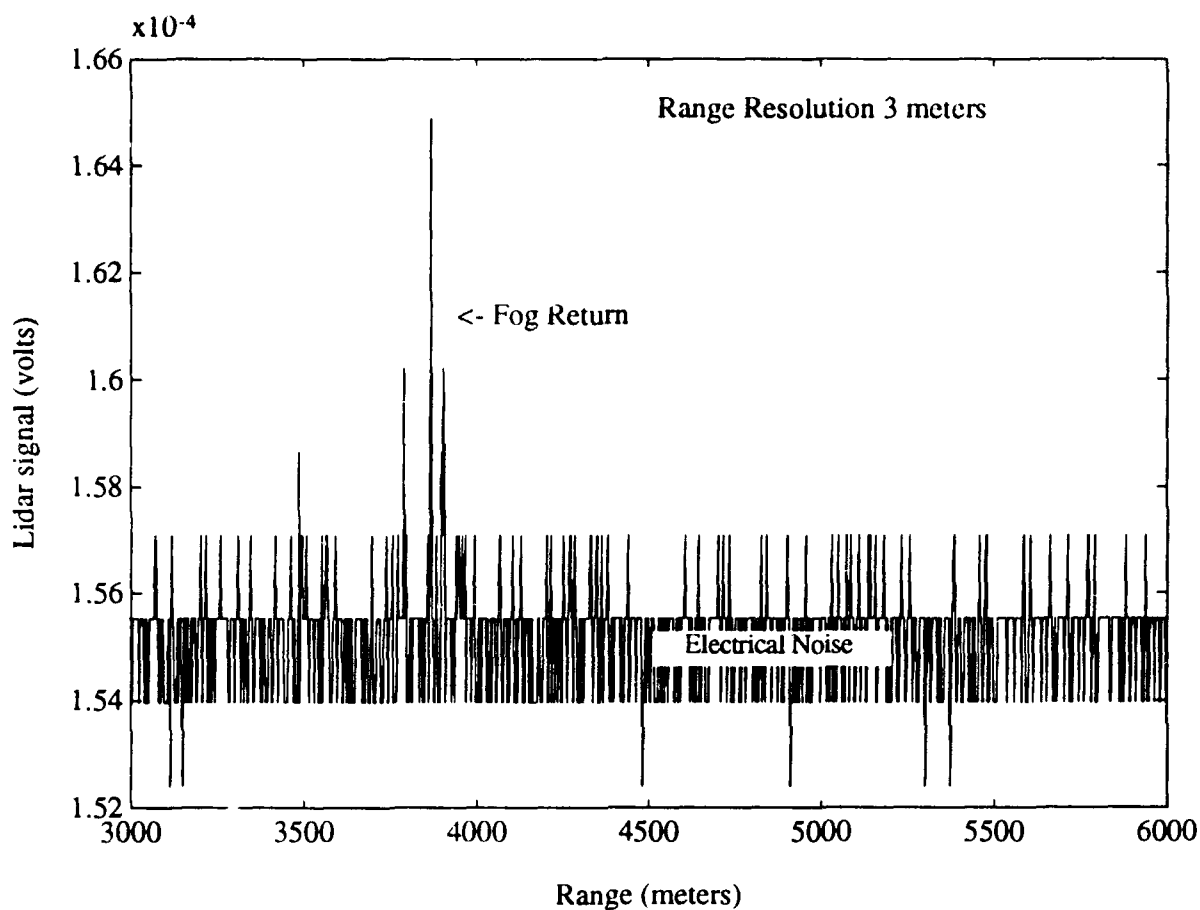
46

Figure 11. Lidar return from fog bank at approximately 2110 hours.

It was noted that, as the evening progressed and the sun set, the background noise decreased as expected, which can be observed by comparing of the noise levels in Figures 9 and 11. The noise floor in Figure 10 was further reduced by averaging two consecutive lidar returns from the same cloud. In order to conduct daytime lidar analysis, the noise levels will have to be reduced by employing a smaller pin-hole as discussed in Chapter III as well as sealing the lidar receiver enclosure better to prevent stray light from entering the lidar receiver box. An averaging technique, such as photon counting, could be employed

47

to reduce the daytime noise levels but typically the pulse repetition rates are in the kiloHertz range to produce good results.

A further discussion of the theoretical day and nighttime lidar ranges is now necessary for comparison purposes. The daytime maximum theoretical range, as derived in Equation (2-27), can be determined by substituting in the design and measured values from Chapter III:

$$r_{max} = \sqrt{\frac{P_o \, \tau \, \beta(r_{max}) \, \sqrt{c \, A_o \, \lambda \, \eta(\lambda)} \, \exp\left[-2 \int_0^{r_{max}} \sigma(r') \, dr'\right]}{\sqrt{8 \, h \, \Delta\lambda \, S_b(\lambda) \, \tau_o(\lambda) \, \Omega_o \, \Delta f}}} \qquad (4\text{-}1)$$

where

r_{max} is the maximum range for the lidar system (meters),
P_o is the lidar system transmitted power
    (0.5 x 10^6 watts, 2 millijoules/4 nanoseconds),
τ is the laser pulse duration (4 nanoseconds),
$\beta(r_{max})$ is the atmospheric volume backscattering coefficient
    (a range of values are given in reference 25 between 1 x 10^{-7} and 1 x 10^{-4}
    meters^{-1} · steradians^{-1}. A value of 6 x 10^{-6} meters^{-1} · steradians^{-1}
    will be assumed),
c is the speed of light (3 x 10^8 meters/second),
A_o is the receiver's effective aperture (0.0165 meter^2),
λ is the laser wavelength (532 x 10^{-9} meters),
$\eta(\lambda)$ is the photomultiplier tube quantum efficiency (15%),
$\sigma(r)$ is the atmospheric volume extinction coefficient (assumed
    to be constant along the path at 2 x 10^{-3} meters^{-1} [Ref. 35]),
h is Planck's constant (6.6266176 x 10^{-34} watts · seconds^2),
$\Delta\lambda$ is the narrowband filter width (0.010 microns),
$S_b(\lambda)$ is the background spectral radiance (10 watts meter^{-2} · steradians^{-1} · micron^{-1}
    [Ref. 22]),
$\tau_o(\lambda)$ is the receiver optics transmittance (assumed to be 0.8),
Ω_o is the receiver solid angle (0.127 x 10^{-3} steradians), and
Δf is the electrical system bandwidth (assumed to be 1 gigaHertz).

The resulting expression for the maximum nighttime range is:

$$r_{max} = 1.0137 \times 10^3 \; exp\left[-2 \times 10^{-3} \; r_{max}\right] \qquad \text{(meters).} \qquad (4\text{-}3)$$

The nighttime maximum theoretical range, as derived in Equation (2-32), can be determined by substituting in the design and measured values from Chapter III:

$$r_{max} = \sqrt{\frac{P_o \, \tau \, A_o \, \tau_o(\lambda) \, \lambda \, \eta(\lambda) \, \beta(r) \; exp\left[-2 \int_0^{r_{max}} \sigma(r') \; dr'\right]}{4 \, h \, \Delta f}} \, . \qquad (4\text{-}4)$$

The resulting expression for the maximum nighttime range is:

$$r_{max} = 6.305 \times 10^3 \; exp\left[-2 \times 10^{-3} \; r_{max}\right] \qquad \text{(meters).} \qquad (4\text{-}5)$$

Equations (4-3) and (4-5) must be solved iteratively to obtain a value for r_{max}. The daytime and nighttime maximum lidar ranges are 0.9 and 3.3 kilometers respectively. The nighttime maximum range seems to be low when comparing it to the lidar return in Figure 11. This should not be possible as the lidar appears to outperform its theoretical limits. Therefore, the overall system bandwidth may be less than 1 gigaHertz or the magnitudes of $\beta(r)$ and $\sigma(r)$ may have been incorrect for the weather conditions. The values chosen for $\beta(r)$ and $\sigma(r)$ reflect the average values for clear air conditions but the conditions may have been better than estimated in the near-field.

49

C. LIDAR INVERSION

A lidar inversion was carried out on the lidar return shown in Figure 10 as it was one of the best lidar returns. The algorithms developed in Chapter II and Appendix B were used to conduct the lidar inversion. It should be noted that the range resolution for the lidar return was 1.2 meters which was well above the high resolution theoretical lidar inversions carried out in Appendix B. Therefore, it will not be the aim to produce an accurate lidar inversion but to demonstrate the capability.

1. Determination of r_o

Before the lidar inversion can progress a value for r_o, the receiver/transmitter overlap range, needs to be determined. This was done theoretically by measuring the displacement of the receiver and transmitter axis, the pin-hole radius in the receiver which will provide the field of view and the transmitter half-angle beam divergence. From Chapter III, the pin-hole diameter was set at 1/8" and the transmitter half angle beam divergence was measured at 0.794 milliradians. The displacement of the two axes was 35.56 centimeters. The graphical solution for r_o showing both the receiver's fields of view and transmitter's beam expansion, in two dimensions, is in Figure 12.

Therefore, the minimum theoretical range at which the receiver's field of view overlaps the transmitter's beam is 104.6 meters. This value will be used in the lidar inversion process.
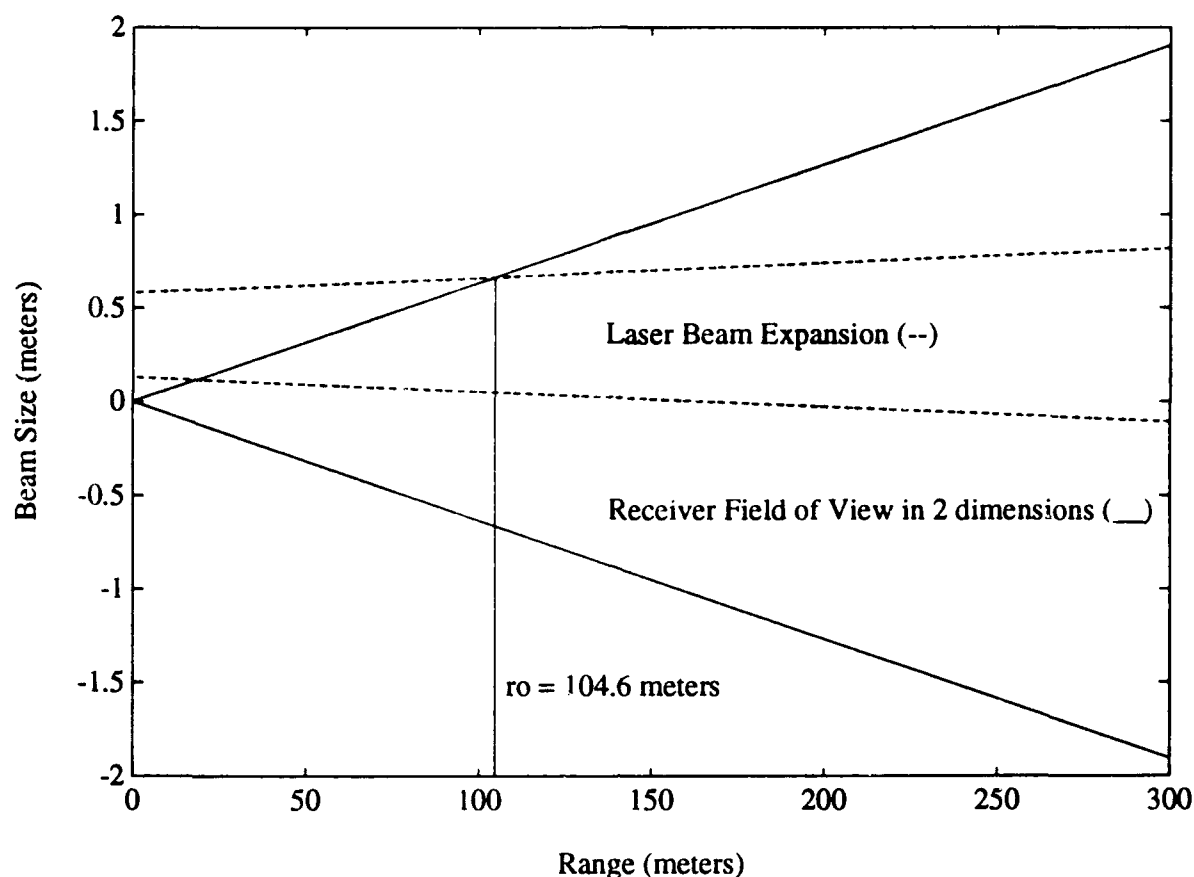
Figure 12. Graphical solution for beam overlap range

2. Lidar inversion

The inversion of the lidar signal is not as straightforward as presented in Chapter II and Appendix B. The determination of the lidar constant, C, from Equation (2-10) can be difficult without prior knowledge for the extinction coefficient profile. If the extinction coefficient is known, then the Lidar equation can be worked backwards to determine the lidar constant which can be used for future lidar inversions. The receiver output signal is a function of the incident power, as presented in Equation (2-25), but in reality there is still an overall system efficiency which must be considered. Therefore, a practical solution to the problem of the lidar constant and receiver efficiency would be to

group these constants together and determine them as a whole by calibrating the lidar against a known extinction coefficient profile. The only problem with this approach would be acquiring the necessary equipment, such as a visioceilometer as described in reference 9.

For the purpose of this lidar inversion, the lidar constant will be set to an arbitrary value. The lidar inversion will be inaccurate at the boundary but the large range resolution will make an accurate lidar inversion impractical anyway. The inverted lidar signal is shown at Figure 13.
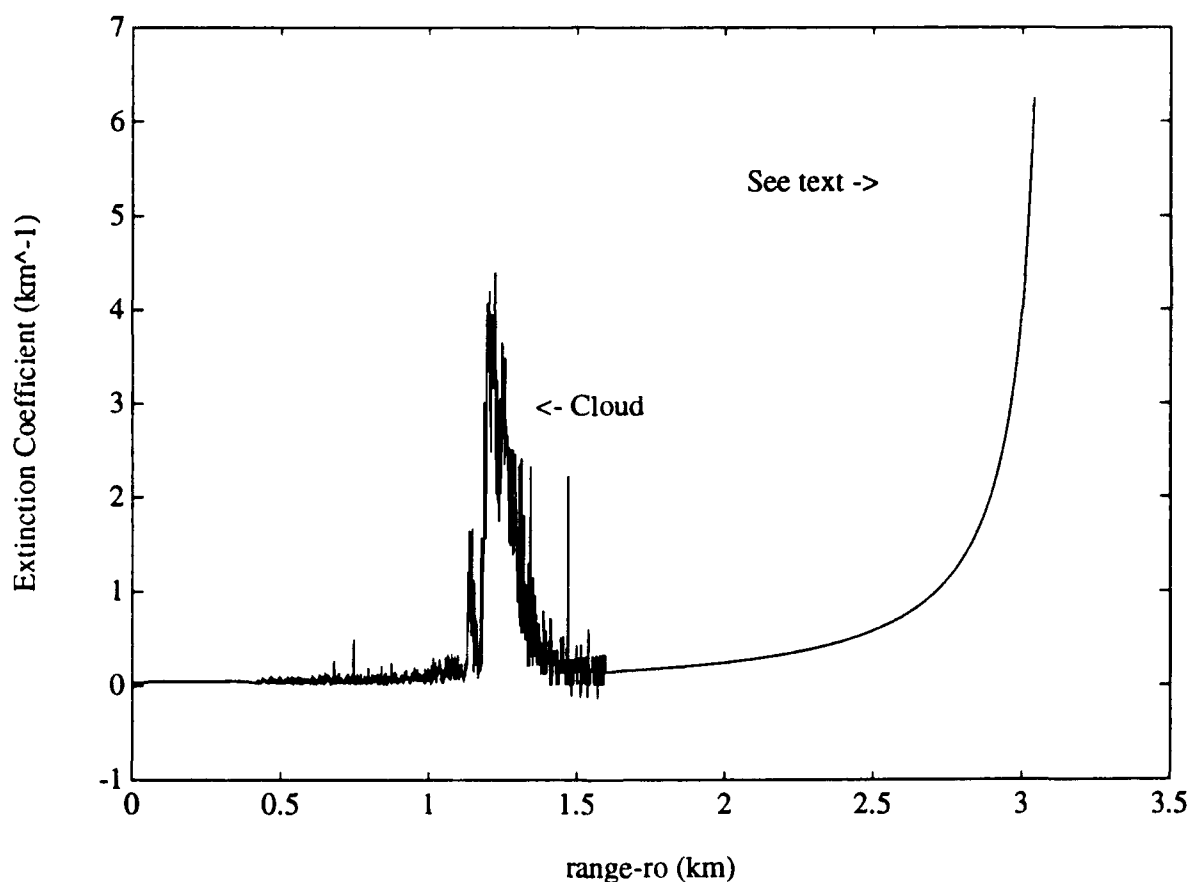

Figure 13. Lidar inversion of Figure 11

The lidar signal, from Figure 11, was first smoothed by piecewise curve fitting to remove the noise from the lidar signal. The cloud return, shown in the center of Figure 11, was left to get a comparison of smoothed and raw lidar data inversion. The piecewise smoothing process was time consuming and investigations into a more practical method are needed. The extinction coefficient profile is shown in Figure 13 and it became very large at the boundary. This is a concern because Figure 11 does not show any returns past the initial cloud return at 1300 meters. Therefore, this is the boundary inaccuracy mentioned earlier due to the arbitrary selection of the lidar constant and the large range resolution.

The cloud irradiated by the lidar in Figure 11 was a light cumulus cloud. The lidar inversion of the cloud region is reasonable since the expected extinction coefficient in cumulus clouds is in the order of 10 kilometer^{-1} [Ref. 36]. The lidar inversion peak measured extinction coefficient was 5 kilometer^{-1} which was close to the expected value. There were errors in the lidar inversion as mentioned earlier but the profile of the cloud was preserved to demonstrate the robustness of the process.

The designed lidar met its objective to provide accurate range information to clouds and fog. A lidar inversion was conducted without prior calibration and it provided reasonable cloud structure data.

The next chapter considers the integration of the lidar with the IRSTD.

V. LIDAR INTEGRATION WITH THE NPS-IRSTD

A. CONCEPT

The general concept for the integration of the lidar with the NPS-IRSTD system appears to be fairly simple but increases in complexity with a detailed analysis. The lidar data would be used initially to obtain range information to those targets identified by the NPS-IRSTD but a secondary aim would be to use the lidar data to correct the IRSTD image for path attenuation. This would permit enhancement of the infrared image for target identification based on accurate temperature measurements. The primary aim of the thesis to obtain range information to atmospheric features, such as clouds and fog, using the lidar was achieved, but in the process enough information was available to determine the actual visibility. The determination of the visibility could be very important for defining the actual atmospheric conditions for future experiments. The ability to correct the NPS-IRSTD image for atmospheric attenuation was not an easy problem as there was no direct correlation available between visible and infrared region extinction. A possible solution has been considered which would require additions to the present lidar system.

B. LOCATION CONSIDERATIONS

A number of details will need to be considered when integrating the lidar into the existing IRSTD system; physical placement of the two systems will be one of the most important. Firstly, as part of the system calibration process, the IRSTD and the lidar will need to be aligned to a predetermined range, defined by operational requirements and the IRSTD system characteristics. The placement of the lidar in relation to the IRSTD will be dependent on the IRSTD's location on board the ship as well as space availability. The following are a number of placement possibilities:

54

1. The ideal placement of the lidar would be inside the IRSTD since there would be no misalignment of optical axis and aiming ambiguity. It would not be possible to fit the designed lidar into the IRSTD's enclosure due to space constraints. It may be reconsidered if the IRSTD and lidar were redesigned to be integrated in the same enclosure.

2. An alternative approach would be to have the lidar placed directly above or below the IRSTD. This would maintain the rotational mechanical axis alignment at the expense of the vertical pointing accuracy. In the limit, as the range becomes much larger than the separation between the lidar and IRSTD, the vertical pointing inaccuracy becomes negligible. The only concern would be the supports for the two sensors and whether they would adversely affect each other's field of view. This would require an operational trade-off study to determine the best option.

3. The most probable approach would be the placement of several lidars aboard the ship. Since real estate on the ship's superstructure will be at prime, the placement of the IRSTD and the lidar on it may pose some problems based on operational priorities. Therefore by using several lidars, each lidar could cover a sector of the ship's perimeter. The coordination of the lidars with the IRSTD may be complex and the pointing accuracy would be a concern which would require detailed study.

There is one location consideration which only applies to the lidar and it deals with the question of the laser eye safety requirements. In the present design, laser eye safety was designed into the system without considering an operational range requirement and this permits unrestricted use. The range requirement, based on the IRSTD detection range and threat, may dictate a noneye safe laser to obtain this range and this may pose operational problems for friendly forces and restrict its use. This problem is similar to the army's concern during OPERATION DESERT STORM with the increased use of laser range finders on the battlefield by both enemy and friendly forces.

The IRSTD's maximum detection range can be assumed to be the horizon for sea skimming missiles and this distance can be expressed in terms of altitude as:

$$\text{distance (in nautical miles)} = 1.14 \, s^{0.5} \tag{5-1}$$

where s is the altitude in feet [Ref. 37]. If the IRSTD is placed on a ship's superstructure at 60 feet above sea level, then the corresponding range is 16.4 kilometer which is much larger than the projected range of the designed lidar. Therefore, to achieve this range, a noneye safe laser will need to be employed.

The lidar's employment may be restricted to those ships operating on the perimeter of a carrier group and further restricted from use in designated aircraft inbound and outbound airspace.

C. RANGE INTEGRATION

The determination of the range to atmospheric features was carried out by using Klett's algorithm as outlined in Chapter II. The time-dependent data obtained from the digital oscilloscope was converted into range data using the speed of light. The lidar system could easily be converted into a laser range finder for hard targets by bypassing the Klett algorithm and using a reflected signal threshold as used in radar.

Once the range to a target has been determined, the display of this information on the NPS-IRSTD console and the frequency of updating need to be addressed. These considerations are dependent on the type of target, which infers its speed, the IRSTD rotation rate, the lidar's target acquisition time and human visual psychophysics.

The lidar inversion process, besides giving range information, provides enough information to determine the visibility. The determination of visibility can be very useful for experimentation purposes as it provides an unambiguous representation of the weather conditions. The visibility or visual range can be determined using the following empirical formula [Ref. 38]:

$$\overline{\sigma(\lambda)} = \frac{3.91}{R_v}\left(\frac{550}{\lambda}\right)^q \tag{5-2}$$

56

where

$\overline{\sigma(\lambda)}$ is the mean value of the wavelength dependent extinction coefficient in kilometers^{-1},

R_v is the visibility or visual range in kilometers,

λ is the wavelength in nanometers, and

q is an empirical constant which is defined as $0.585 (R_v)^{1/3}$ for $R_v \leq 6$ kilometers or $= 1.3$ for average seeing conditions [Ref. 39].

It has been noted that Equation (5-2) becomes inaccurate above 2 microns producing a significant underestimation of the extinction coefficient [Ref. 39]. Therefore, visibility estimates in the visible spectrum cannot adequately be correlated to those for the infrared spectrum.

D. INFRARED EXTINCTION COEFFICIENT

Since the determination of the infrared extinction becomes difficult when using visible spectrum data, the best approach would be to use a laser which operates in the region of the infrared sensor. The extinction coefficient can be directly determined using the Klett algorithm and the infrared image can be directly enhanced. There are a number of disadvantages in this approach which directly influenced the choice of a laser for this thesis:

1. The power law backscattering coefficient and extinction coefficient relationship is not as strong in the infrared region as it is in the visible spectrum (as discussed in Chapter II). Therefore, the extinction coefficient is harder to determine in the infrared spectrum.

2. The possibility of blinding the NPS-IRSTD due to the near-field backscattered radiation is a concern if a 3-5 micron laser was to be employed in the lidar. The use of a laser line filter on the IRSTD may be considered to prevent blinding or damage.

3. There was no laser available at the school operating in the 3-5 micron region for the lidar thesis. Those commercial lasers available which could operate in this region are deuterium fluoride, helium neon (4-5 microns reported by one manufacturer), erbium:YAG (2.94 microns) and a few tunable lead salt semiconductor lasers [Ref. 40].

1. Apparent Temperature Solution

A possible solution for the determination of the infrared extinction coefficient would be the use of clouds or fog infrared temperatures. In the infrared spectrum, satellite remote sensing uses the fact that clouds can be approximated as blackbodies with a definable temperature and this approach can be applied in this application. A cloud's temperature can be obtained from the NPS-IRSTD but this temperature would be the apparent temperature, since there would be path attenuation of the cloud emission. With a modified lidar, the path temperature up to and including the cloud or fog boundary could be determined. The mean path transmittance can then be calculated assuming that the cloud section imaged by the NPS-IRSTD radiates as a blackbody into a hemisphere with the temperature obtained from the lidar.

There are a number of lidar methods used to measure the path temperature profiles; these include: [Ref. 41]

1. Raman scattering,

2. differential absorption, and

3. doppler broadening.

a. Raman Scattering

Raman scattering is the weakest of the scattering phenomena but it provides a means of identifying the scattering due to a particular molecule regardless of the wavelength of the incident radiation, which makes it attractive for fixed wavelength lasers. Raman scattering is inelastic scattering and is developed from the quantum theory of scattering. It is characterized by a series of scattered wavelengths λ_{laser}, $\lambda_{laser} \pm \lambda_1$, $\lambda_{laser} \pm \lambda_2$, etc. where λ_1, λ_2, etc. refer to the energy differences in the molecular species in the laser beam path. The longer wavelength shifted lines are referred to as Stokes lines while

58

the shorter wavelength shifts are referred to as anti-Stokes lines. Matched pairs of shifted lines (i.e., $\lambda_{laser} \pm \lambda_2$) have roughly the same intensity. The radiating wavelength will either gain or lose energy from the incident molecule's rotational and/or vibration states. The scattered light spectrum will have a strong intensity at the original wavelength and much weaker intensities at the shifted wavelengths. This molecular dependent shift in the wavelengths is called the characteristic Raman spectrum and, when applied to remote sensing, this phenomenon is referred to as Raman scattering.

The pure rotational Raman spectrum has been used for lidar applications because the magnitude of the spectral lines is two orders of magnitude greater than the vibrational-rotational spectral lines. The larger spectral magnitudes make the pure rotational Raman spectrum easier to measure than the weaker vibrational-rotational spectrum without loss of information. The intensity of the pure rotational Raman spectral lines can be written as [Ref. 42]:

$$I(J,T) = I_o \frac{c}{\lambda_J^4} g_I \frac{BN_o}{kT} (2J + 1) S(J) \exp\left[\frac{-B J (J + 1)}{kT}\right] \qquad (5-3)$$

where

    J is the Stokes and anti-Stokes Raman rotational quantum number,
    I_o is the incident intensity of the laser beam,
    λ_J is the Raman spectral wavelength which is molecule dependent,
    c is the speed of light,
    g_I is the statistical weight due to nucleus spin,
    B is the rotational constant of the incident molecule,
    N_o is the number of atoms in the ground state,
    k is Boltzmann's constant, and
    T is the temperature of the molecule.

The product of the S(J) and the degeneracy factor (2J + 1) can be written for the Stokes and anti-Stokes spectral lines as:

$$(2J + 1) \, S(J) \; = \; \frac{(J + 1)(J + 2)}{(2J + 3)} \qquad \text{(Stokes Branch)} \qquad (5\text{-}4)$$

or

$$(2J + 1) \, S(J) \; = \; \frac{J \, (J + 2)}{(2J - 1)} \qquad \text{(anti-Stokes Branch).} \; (5\text{-}5)$$

The temperature dependence of the intensity of the Raman scattered wavelength can be clearly seen from Equation (5-3). There are a number of Raman scattering approaches for measuring temperature [Refs. 42, 43 and 44]. One such approach uses two rotational Raman scattering molecular lines from which a simple temperature dependent expression can be written [Ref. 42]:

$$R(T) \; = \; \exp\left(\frac{\alpha}{T} + \beta\right) \qquad\qquad (5\text{-}6)$$

where

R(T) is the ratio of the Raman scattered intensities or received powers,
α is the ratio of rotational energies,
T is the temperature, and
β is ratio of the difference Raman S(J) functions.

The α term can be written as:

$$\alpha \; = \; \frac{E_{rot}(J_1) - E_{rot}(J_2)}{k} \qquad\qquad (5\text{-}6)$$

where

E is the mean rotational energy of the Raman scattered wavelength,
J is the Raman quantum number, and
k is Boltzmann's constant.

The β term can be expressed as:

60

$$\beta = \ln\left(\frac{S(J_1)}{S(J_2)}\right) \qquad (5\text{-}7)$$

where the Raman S(J) function can be determined from Equation (5-4) or (5-5) depending on which Raman spectral wavelength is observed.

In the visible spectrum, the popular molecular species used for Raman scattering are oxygen and nitrogen because of their uniform concentrations in the atmosphere. The only problem involved in this approach is the separation of the Raman scattered lines without significant loss of signal strength. In the past, this has been a significant problem but now specially developed laser line notch filters, called holographic notch filters, have alleviated this problem. These filters have a very narrow bandwidth which make them ideal for the removal of the transmitting laser wavelength from the backscattered signal. An optical grating could then be used to observe the desired Raman scattering wavelength. This approach to temperature measurement would be easy to implement on this lidar as it only requires modification to the lidar receiver.

b. Differential Absorption

The differential absorption method used for the measurement of temperature profiles requires two laser wavelengths, one on a molecular species absorption wavelength and the other slightly off. The ratio of the backscattered signals is used to obtain information about the path temperature because the absorption coefficient is temperature dependent. The two wavelengths used need to be close enough together so that the transmittance along the path is approximately the same for each wavelength and the lasers have the same energy output to remove these dependencies from the ratio of the two backscattered signals. The typical absorption wavelengths chosen have been those of water vapor or oxygen lines [Ref. 45], but the best choice would probably be the oxygen line since it is uniformly mixed in the atmosphere.

61

In order to use this approach both the lidar receiver and transmitter would have to be modified. A second laser with the same energy output as the Nd:YAG laser would be needed as well as a modifications to the receiver.

c. Doppler Broadening

The doppler broadening approach to temperature measurement uses the doppler molecular species broadening of the lidar backscattered frequency spectrum. This spectrum is composed of a large aerosol component and weak molecular component. The molecular component has a Gaussian lineshape which is related to temperature. A scanning Fabry-Perot interferometer could be used to measure the spectral linewidth between the half-width half-maximum points and thereby obtain a temperature [Ref. 46]. If the doppler broadening is known for a reference temperature, then the following expression can be written [Ref 5]:

$$\Delta\lambda(T) = \Delta\lambda(T_{ref}) \left[\frac{T_{ref}}{T}\right]^{0.5} \tag{5-8}$$

where

$\Delta\lambda(T)$ is the lidar spectral linewidth at temperature T, and
$\Delta\lambda(T_{ref})$ is the lidar spectral linewidth at a calibrated reference temperature T_{ref}.

This approach would be difficult to implement since the doppler broadening varies along the path and the interferometer may not be able to scan fast enough to determine the frequency spectrum along the path. The receiver would need to be range gated to obtain temperature measurements at specified ranges such as a cloud boundary. The boundary temperature would be used for the apparent temperature solution for the path average infrared extinction coefficient and only requires additions to the receiver. This

62

approach would not lend itself well for further studies of path temperatures as it would be very slow to obtain temperature profiles over a long path.

The next chapter will present the thesis conclusions and recommendations for future further lidar work.

VI. CONCLUSIONS AND RECOMMENDATIONS

A lidar was designed and manufactured and the lidar was able to range atmospheric features as demonstrated in Chapter IV. The theoretical maximum range for the lidar is approximately 3.3 kilometers by night and 0.9 kilometer by day. These ranges are well below the required detection range for integration with the IRSTD, which was determined to be 16.4 kilometers for targets on the horizon. Never-the-less, the lidar did demonstrate a ranging capability and an inversion of a cloud lidar return did provide an estimate of a cloud structure. The lidar is mounted on a pedestal which allows azimuth and elevation pointing.

There are many improvements to be made on the lidar which were discovered during the course of the design, manufacturing and evaluation process:

1. A single lens was used to expand the laser beam to fill the telescope's secondary mirror but there was a problem with overfill, possibly due to measurement errors. A double lens beam expander should be considered to provide a fine adjustment of the beam expander focal length in order to properly fill the telescope's secondary mirror.

2. The laser box mirror and lens mounts used, except one, were all non-precision mounts and to get the correct laser beam height and alignment employed a trial and error method for the placement of shims. This was very time consuming and, if any further work is planned for the laser box, adjustable precision optical mounts should be purchased.

3. The lidar receiver's field of view can also be restricted to improve the daytime maximum range by further reducing the background scene noise. This would not provide any increased nighttime range.

4. The daytime noise levels in the lidar receiver are a concern and need to be investigated as they restrict the maximum daytime detection range.

5. If the lidar daytime receiver noise levels can be reduced, then a photomultiplier tube amplifier could be used to amplify the daytime lidar signals to further increase detection range.

6. A logarithmic amplifier could be placed at the output of the lidar receiver to compress the lidar signal. This amplifier would only amplify the weak long-range signals while leaving the near-field return in its original form. By amplifying the long range signals, more information about long-range atmospheric features could be obtained.

7. The lidar system needs to be calibrated, as discussed in Chapter IV, to determine the value for the lidar constant. Without a calibration of the lidar system, accurate path extinction coefficient information will not be possible.

This lidar is viewed as a stepping stone for further research of the atmosphere. A standard lidar inversion technique, the "Klett" method, was used to demonstrate the lidar's ability to provide information on the path extinction coefficient both using theoretical and real lidar data. Further work and refinement is needed to determine the best lidar inversion technique and then to apply this technique to the lidar measurements taken in Chapter IV to see if better results can be achieved. In order to take temperature and humidity atmospheric measurements in the future, an investigation will need to be conducted on the best method to be used from those described in Chapter V and from more recent sources. If the Raman scattering approach is to be used, a holographic notch filter should be purchased.

The lidar system achieved its goal to provide range information from atmospheric features. There has been identified a number of areas for improvement in order to enhance the lidar's accuracy and range as well as for follow-on research.

This thesis has been a challenging and enlightening experience in the area of lidar theory, design and manufacturing.

APPENDIX A

ANALYSIS OF KLETT EQUATION

This appendix presents an analysis of the Klett equation and a method by which an expression for the extinction coefficient boundary value, $\sigma(r_m)$, can be determined. The Klett equation, as discussed in Chapter 2, produces a stable solution for the lidar equation by determining $\sigma(r_m)$ and integrating the Klett equation backwards from r_m to r to obtain the extinction coefficient along the path, $\sigma(r)$. The value for $\sigma(r_m)$ can be approximated by relating it to the signal strength $S(r_m)$. The general form of the Klett equation, as presented in Chapter 2 as Equation (2-8), is:

$$\sigma(r) = \frac{\exp\left[(S(r) - S(r_m))/k\right]}{\dfrac{1}{\sigma(r_m)} + \dfrac{2}{k}\displaystyle\int_r^{r_m} \exp\left[(S(r') - S(r_m))/k\right]\, dr'} \tag{A-1}$$

where

       $\sigma(r)$ is the extinction coefficient along a path at range r,
       $\sigma(r_m)$ is the extinction coefficient boundary value at range r_m,
       $S(r)$ is the logarithmic range adjusted power at range r, $S(r) \equiv \ln(r^2 P(r))$,
       $S(r_m)$ is the logarithmic range adjusted power at the boundary range r_m, and
       k is the exponent used in the relationship $\beta(r) = \text{Constant } \sigma(r)^k$.

The first step to obtain an expression for $\sigma(r_m)$ in terms of $S(r_m)$ is to make a variable substitution into Equation (A-1) and then solve the resulting equation as a linear differential equation as shown below:

1. A new variable F(r) and its derivative are defined in terms of the denominator of Equation (A-1).

$$F(r) = 1 + \frac{2 \; \sigma(r_m)}{k} \int_r^{r_m} \exp \left[(S(r') - S(r_m))/k \right] \; dr' \tag{A-2}$$

$$\frac{d \; F(r)}{dr} = \frac{-2 \; \sigma(r_m)}{k} \exp \left[(S(r) - S(r_m))/k \right] \; . \tag{A-3}$$

2. After the substitution of Equations (A-2) and (A-3) into Equation (A-1), the resulting expression is:

$$\sigma(r) = \frac{-k}{2 \; F(r)} \frac{d \; F(r)}{dr} \; . \tag{A-4}$$

3. Equation (A-4) can now be rewritten as a linear differential equation.

$$\frac{d \; F(r)}{dr} + \frac{2}{k} \sigma(r) \; F(r) = 0 \tag{A-5}$$

4. The solution to the differential equation can be obtained by using an integrating factor. The choice of the lower limit of integration for the integrating factor is arbitrary.

$$\text{Integrating Factor:} \quad \exp \left[\frac{2}{k} \int^{r'} \sigma(r) \; dr \right] \tag{A-6}$$

$$\frac{d}{dr} \left(F(r) \exp \left[\frac{2}{k} \int^{r'} \sigma(r) \; dr \right] \right) = 0 \tag{A-7}$$

$$\int_{r_0}^{r_m} \frac{d}{dr} \left(F(r) \exp \left[\frac{2}{k} \int^{r'} \sigma(r) \; dr \right] \right) dr' = 0 \tag{A-8}$$

$$F(r_m) \exp \left[\frac{2}{k} \int_{r'}^{r_m} \sigma(r) \; dr \right] - F(r_0) \exp \left[\frac{2}{k} \int_{r'}^{r_0} \sigma(r) \; dr \right] = 0 \tag{A-9}$$

5. The selection of the limit of integration, r´, should now be considered in order to simplify the analysis. By selecting r´ = r_m and noting that $F(r_m) = 1$ as determined from Equation (A-2), the resulting expression for Equation (A-9) becomes:

$$\exp\left[\frac{2}{k}\int_{r_m}^{r_o}\sigma(r)\,dr\right] = \frac{1}{F(r_o)} \quad .$$

(A-10)

6. If the natural logarithm is taken of Equation (A-10) and the limits of integration for the integral are switched, the resulting expression is:

$$\int_{r_o}^{r_m}\sigma(r)\,dr = \frac{k}{2}\,\ln(F(r_o)) \quad .$$

(A-11)

By substituting Equation (A-2) for the expression for $F(r_o)$ into Equation (A-11), the resulting expression is the same as that used by Klett [Ref. 20]:

$$\int_{r_o}^{r_m}\sigma(r)\,dr' = \frac{k}{2}\ln\left[1 + \frac{2\,\sigma_m}{k}\int_{r_o}^{r_m}\exp\left[(S(r') - S(r_m))/k\right]\,dr'\right]$$

(A-12)

or, using a more compact notation:

$$\int_{r_o}^{r_m}\sigma(r)\,dr' = \frac{k}{2}\ln\left(1 + I\,\Omega_m\right)$$

(A-13)

where

$$I = (r_m - r_o)^{-1}\int_{r_o}^{r_m}\exp\left[(S(r') - S(r_m))/k\right]\,dr'$$

(A-14)

68

and

$$\Omega_m = \frac{2 \; \sigma(r_m)\,(r_m - r_o)}{k} \quad .$$ (A-15)

Using the assumption that the average extinction coefficient over the range 0 to r_m is equal to that over the range r_o to r_m, which is reasonable if $r_o \ll r_m$, additional progress can be made on Equation (A-13).

1. The average path extinction coefficient is approximated as:

$$\frac{1}{r_m} \int_0^{r_m} \sigma(r)\,dr \approx \frac{1}{(r_m - r_o)} \int_{r_o}^{r_m} \sigma(r)\,dr \quad .$$ (A-16)

2. The expression for $S(r_m)$ is derived from Equations (2-1) and (2-3).

$$S(r_m) = \ln\left(P_o \frac{c\tau}{2} A \text{ Constant } \sigma(r_m)^k \exp\left[-2 \int_0^{r_m} \sigma(r)\,dr \right] \right)$$ (A-17)

$$S(r_m) = \ln\left(P_o \frac{c\tau}{2} A \text{ Constant} \right) + k \ln(\sigma(r_m)) - 2 \int_0^{r_m} \sigma(r)\,dr$$ (A-18)

$$S(r_m) = C + k \ln(\sigma(r_m)) - 2 \int_0^{r_m} \sigma(r)\,dr \quad .$$ (A-19)

3. The integral term in Equation (A-19) can be rewritten using the equivalence relationship from Equation (A-16).

$$S(r_m) = C + k \ln(\sigma(r_m)) - \frac{2\,r_m}{(r_m - r_o)} \int_{r_o}^{r_m} \sigma(r)\,dr \quad .$$ (A-20)

4. The integral term in Equation (A-20) can be removed by the substitution of Equation (A-13) and the resulting expression is:

$$S(r_m) - C = k \ln(\sigma(r_m)) - \frac{2 r_m}{(r_m - r_o)} \frac{k}{2} \ln(1 + I \Omega_m) \qquad \text{(A-21)}$$

5. By adding to both sides,

$$\ln\left(\frac{2(r_m - r_o)}{k}\right) \qquad \text{(A-22)}$$

the final expression for $\sigma(r_m)$ in terms of $S(r_m)$ is now in the form presented as Equation (2-9).

$$\frac{S(r_m) - C}{k} + \ln\left(\frac{2(r_m - r_o)}{k}\right) = \ln(\Omega_m) - \frac{r_m}{(r_m - r_o)} \ln(1 + I \Omega_m) \qquad \text{(A-23)}$$

APPENDIX B

THEORETICAL LIDAR INVERSION

A. INTRODUCTION

This appendix examines the theoretical aspects of the "Klett" method for lidar inversions. For the analysis, eight known extinction profiles ($\sigma(r)$) are used to generate a $S(r)$ or logarithmic range adjusted power profile. Then using the Klett inversion method, the $S(r)$ profile was inverted to obtain the extinction coefficient profile. A comparison of the inverted to the known extinction profile was made using low and high range resolution data. A brief second analysis was conducted on selected extinction profiles by adding Gaussian white noise on top of the received lidar signal to determine the effect of noise on the inversion process.

B. EXTINCTION PROFILES

In order to test the Klett inversion algorithm, a number of extinction profiles were obtained fiom Mr. William Lentz, a physicist at the Naval Postgraduate School, who has conducted previous work in this field and has worked with Mr. Klett. The extinction profiles chosen were used by Mr. Lentz in his work in lidar inversions and are typical of extinction profiles which could be encountered.

The first set of extinction profiles, curves a and b shown in Figure 14, deal with the simplest case, in which the extinction coefficient is constant. The next set of extinction coefficients, curves c and d shown in Figure 15, shows a lidar profile going from a low to high visibility (e.g., out of fog bank or cloud). The constant extinction coefficient out to 255 meters simulates the Klett assumption that the extinction coefficient from range 0 to r_0 is constant and approximately equal to the extinction coefficient at range r_0, as described in

71

Appendix A. The range r_0 is the minimum range at which the lidar transmitter and receiver fields of view overlap and meaningful lidar data can be taken.

The next set of extinction profiles, curves e and f shown in Figure 16, are the inverse of Figure 15. In this case, the lidar profile simulates going into a cloud or fog while the lidar signal fades into noise. As in the Figure 15, the Klett assumption concerning the constant nature of the extinction coefficient over the range 0 to r_0 is used. The final set of extinction profiles, curves g and h shown in Figure 17, consider the case where the lidar is able to penetrate through a cloud or fog bank and obtain data from the other side.
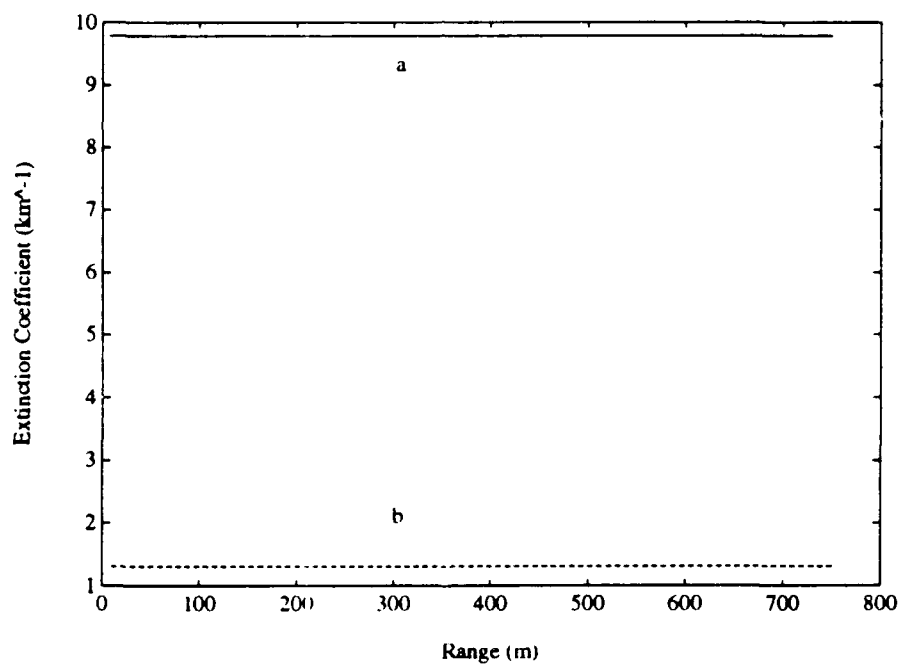
Figure 14. Constant Extinction Coefficient curves a and b.
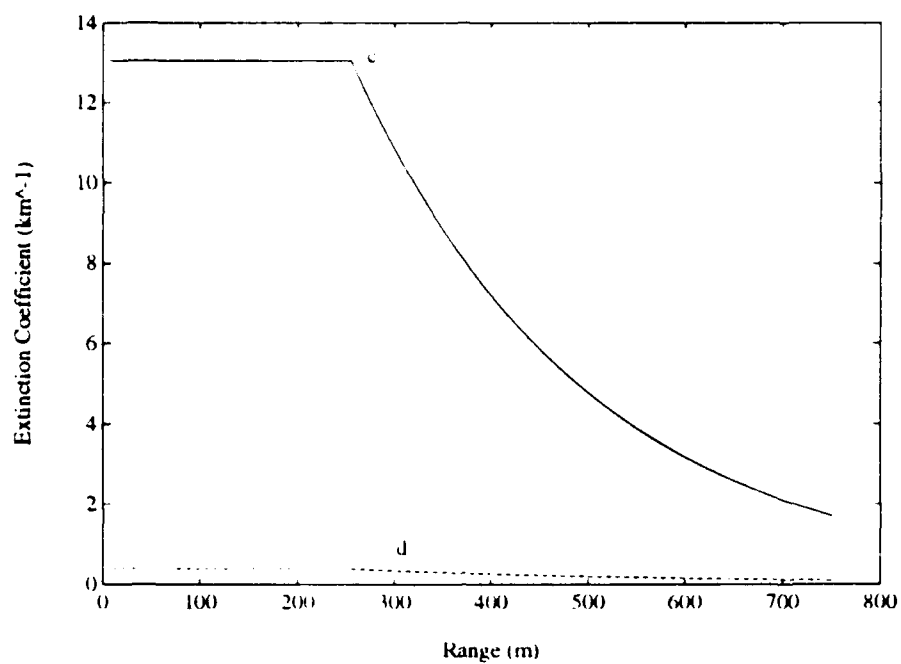
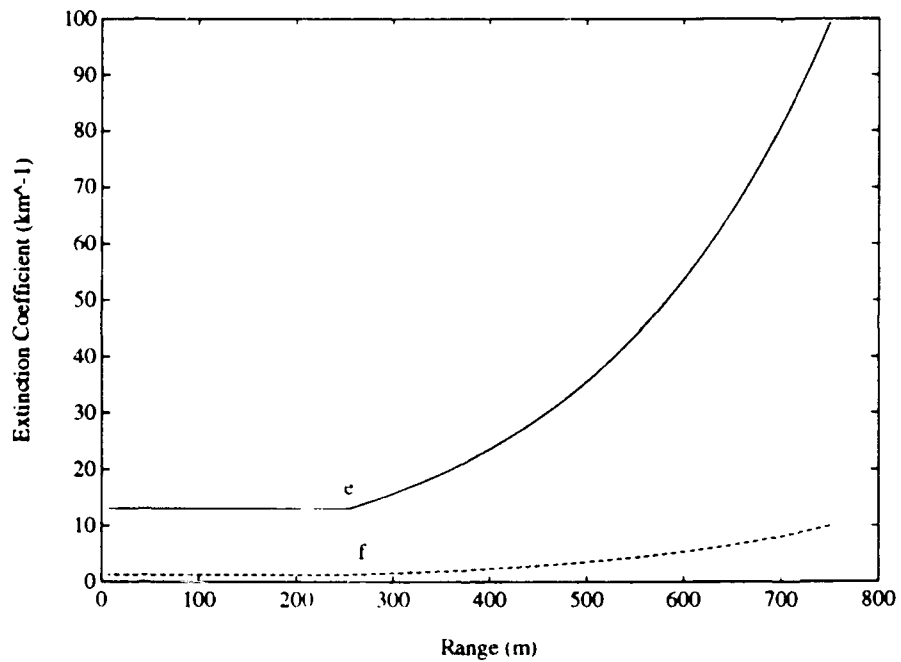Figure 15. Exponentially Decreasing Extinction Coefficient curves c and d.

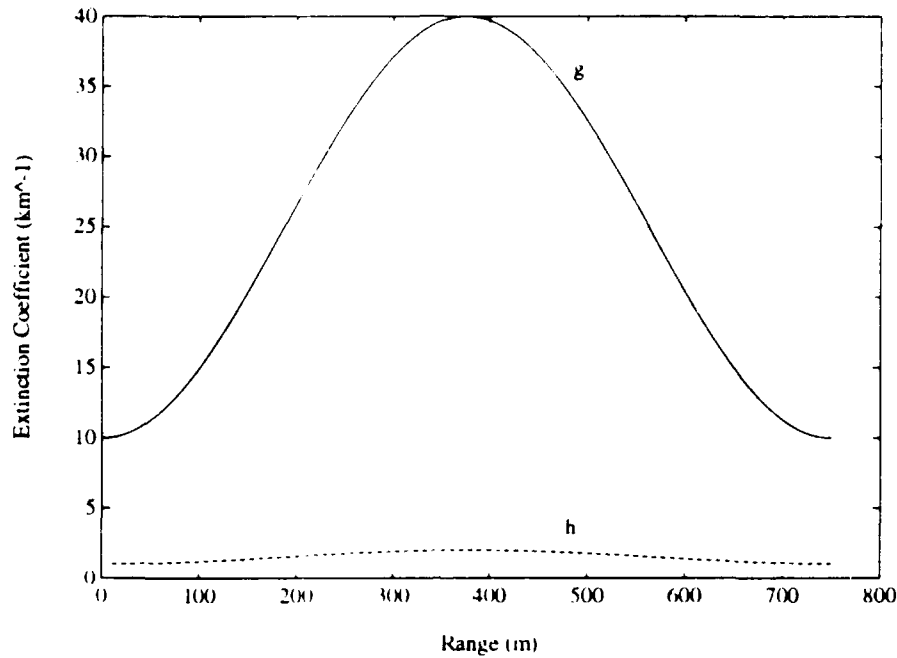Figure 16. Exponentially Increasing Extinction Coefficient curves e and f.

73

Figure 17. Dynamic Range Extinction Coefficient curves g and h.

C. ANALYSIS

The lidar theoretical inversion program, listed in Section D, was written in the MATLAB numeric computation software programming language. The process used to invert a lidar return was:

1. Convert the known extinction coefficient profile into a S(r) profile using the general form of Equation (A-17) rewritten as:

$$S(r) = \ln\left(P_o \frac{c\tau}{2} A \text{ Constant}\right) + k \ln(\sigma(r)) - 2\int_0^r \sigma(r)\, dr \cdot \qquad \text{(B-1)}$$

The $\ln(P_o\, c\tau/2\, A$ Constant) term is a constant and can be set to any arbitrary value. The determination of this value is unimportant since it will be canceled out during the inversion process.

2. Invert the generated S(r) profile using the selection criteria for the extinction coefficient boundary value ($\sigma(r_m)$) described in Chapter II.

74

3. Compare the known extinction coefficient profile to inverted extinction coefficient profile.

The lidar inversion algorithm was applied to simulated low-resolution (7.5 meter) and high-resolution (0.15 meter) range data. The range resolution is determined by the sampling rate used to convert the analog backscattered return to digital form. The low-resolution case was provided by Mr. William Lentz with the sample extinction profiles where the sampling rate used was 20 megaHertz [Ref. 9]. The high-resolution case was analyzed because of its importance to the actual lidar inversion to be theoretically achieved in this thesis. The backscattered return was initially planned to be digitized using a digitizing oscilloscope which had a sampling rate of 1 gigasample per second. The time domain sampling interval is 1 nanosecond between samples which converts into 0.3 meters between samples, but this is round-trip time and it should be divided by two to get the range from which the backscattered signal originated. Therefore, the actual range resolution is 0.15 meters.

The lidar inversions of the S(r) files, generated from the extinction coefficient curves *a–h*, shown at Figures 15–17, were conducted using both the low and high-resolutions. It was noted during the lidar inversion analysis that most of the inverted profiles were very close to the actual extinction profiles. When initially displaying the data, it appeared that one or more profiles are missing but in fact they were actually coincident. Therefore, it was decided to display only the differences between the inverted and actual extinction coefficient profiles so as not to confuse the reader. The following observations were made from each lidar inversion:

75

1. Figure 18. This figure shows the difference between the low and high-resolution
   inversions of the S(r) file, generated from curve a from Figure 14, and the actual
   curve a.. The high range resolution inversion followed the actual extinction profile
   much better than the low-resolution case. The low-resolution inversion deviation is
   mainly due the numerical integration methods which approach the continuous integral
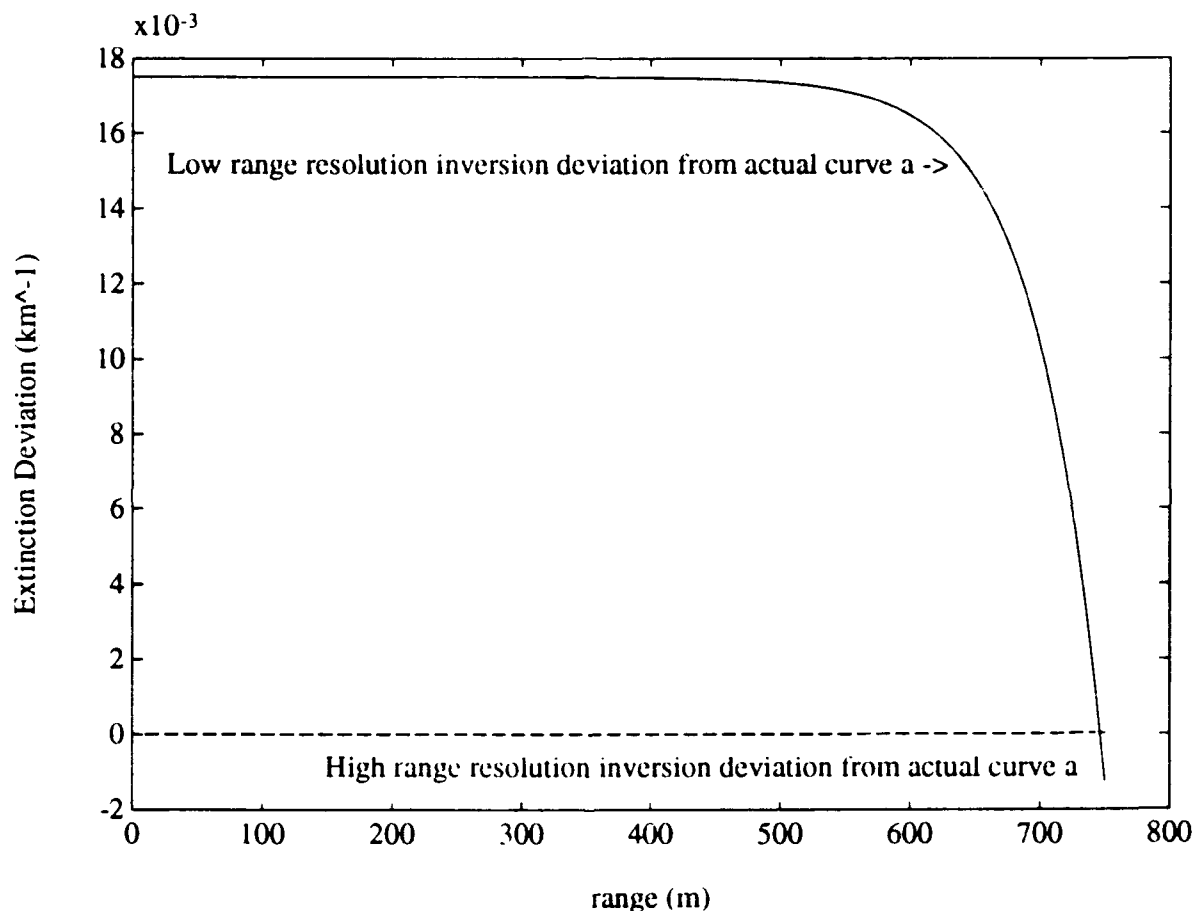   solution when the interval width becomes small enough.

x10⁻³

Figure 18. Extinction Coefficient deviations from the actual values (Figure 14 curve a) by the
the high and low-resolution inversions.

76

2. Figure 19. This figure shows the difference between the low and high-resolution inversions of the S(r) file, generated from curve *b* of Figure 14, and the actual curve *b*. The high range resolution inversion followed the actual extinction profile better but there was no real advantage for using the high-resolution to invert the S(r) file when the low-resolution inversion worked just as well. Therefore for high constant visibility conditions, low-resolution data acquisition will provide accurate results.
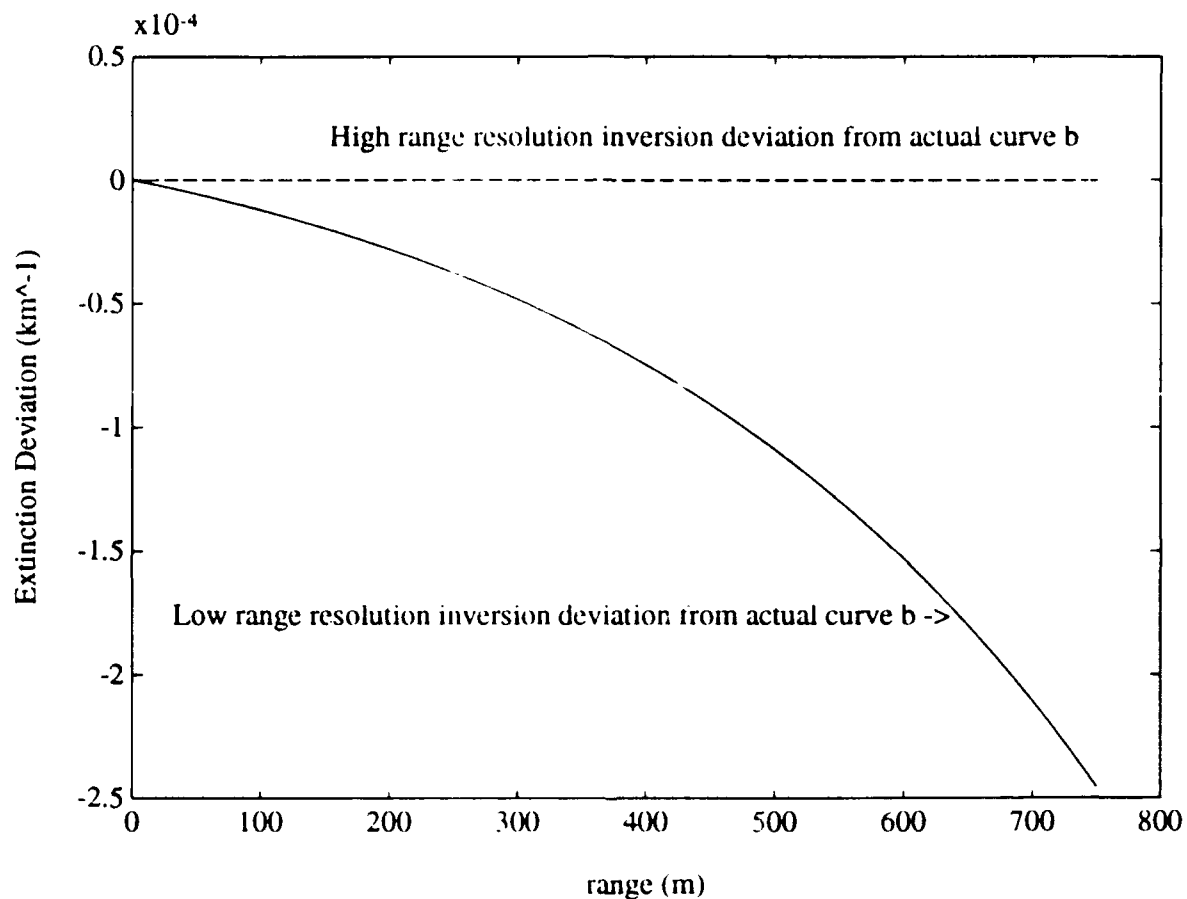

Figure 19. Extinction Coefficient deviations from the actual values (Figure 14 curve *b*) by the the high and low-resolution inversions.

3. Figure 20. This figure shows difference between the low and high-resolution inversions of the S(r) file, generated from curve *c* from Figure 15, and the actual curve *c*. As noted in Figure 18, the high-resolution inversion provided a more accurate representation of the actual Extinction Coefficient profile. It was noted that the maximum extinction deviation is much larger than in the two previous figures, Figure 18 and 19.
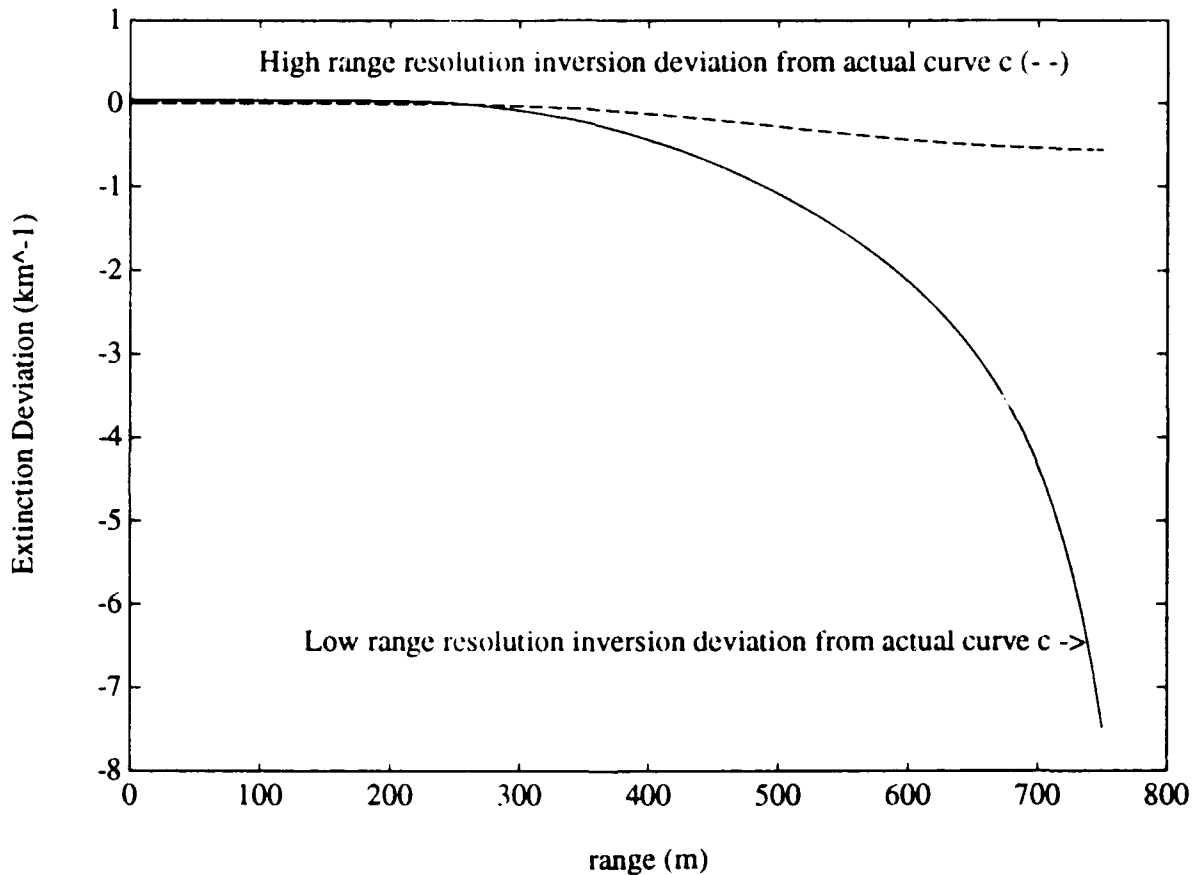

Figure 20. Extinction Coefficient deviations from the actual values (Figure 15 curve *c*) by the the high and low-resolution inversions.

4. Figure 21. This figure shows the difference between the low and high-resolution inversions of the S(r) file, generated from curve d from Figure 15, and the actual curve d. As noted in Figure 19, there was no advantage in using the high-resolution inversion over the low-resolution inversion, since the maximum deviation was in the order of 10^{-6} km^{-1}.
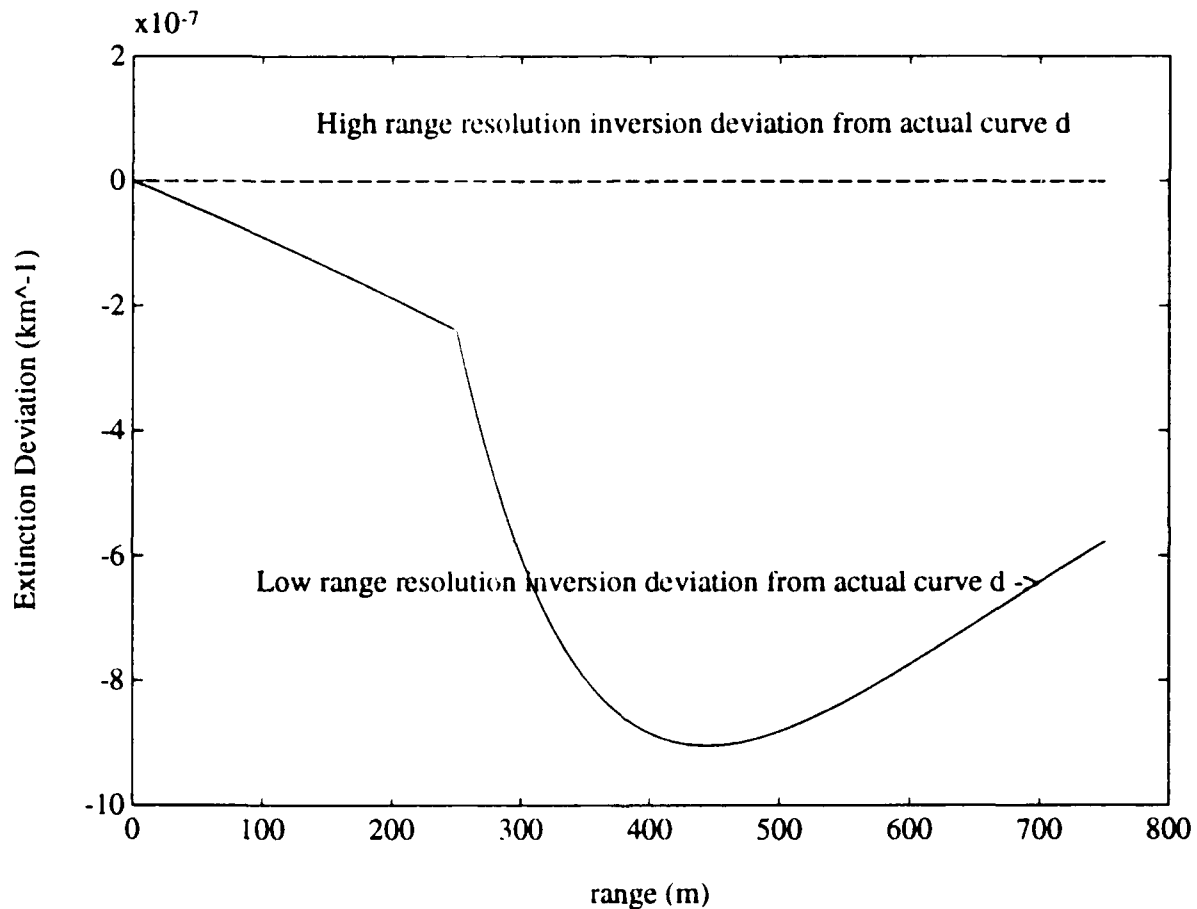

Figure 21. Extinction Coefficient deviations from the actual values (Figure 15 curve d) by the the high and low-resolution inversions.

5. Figure 22. This figure shows the difference between the low and high-resolution inversions of the S(r) file, generated from curve e from Figure 16, and the actual curve e. The large deviation was noted in both the high and low-resolution inversions. This is due to the Low Visibility algorithm. The algorithm becomes sometimes unreliable, as also noted by Klett. The simple assumption that the mean of the extinction coefficient is equal to the boundary value extinction coefficient, Equation (2-16), is always not valid when there is a large dynamic range of the extinction coefficient.
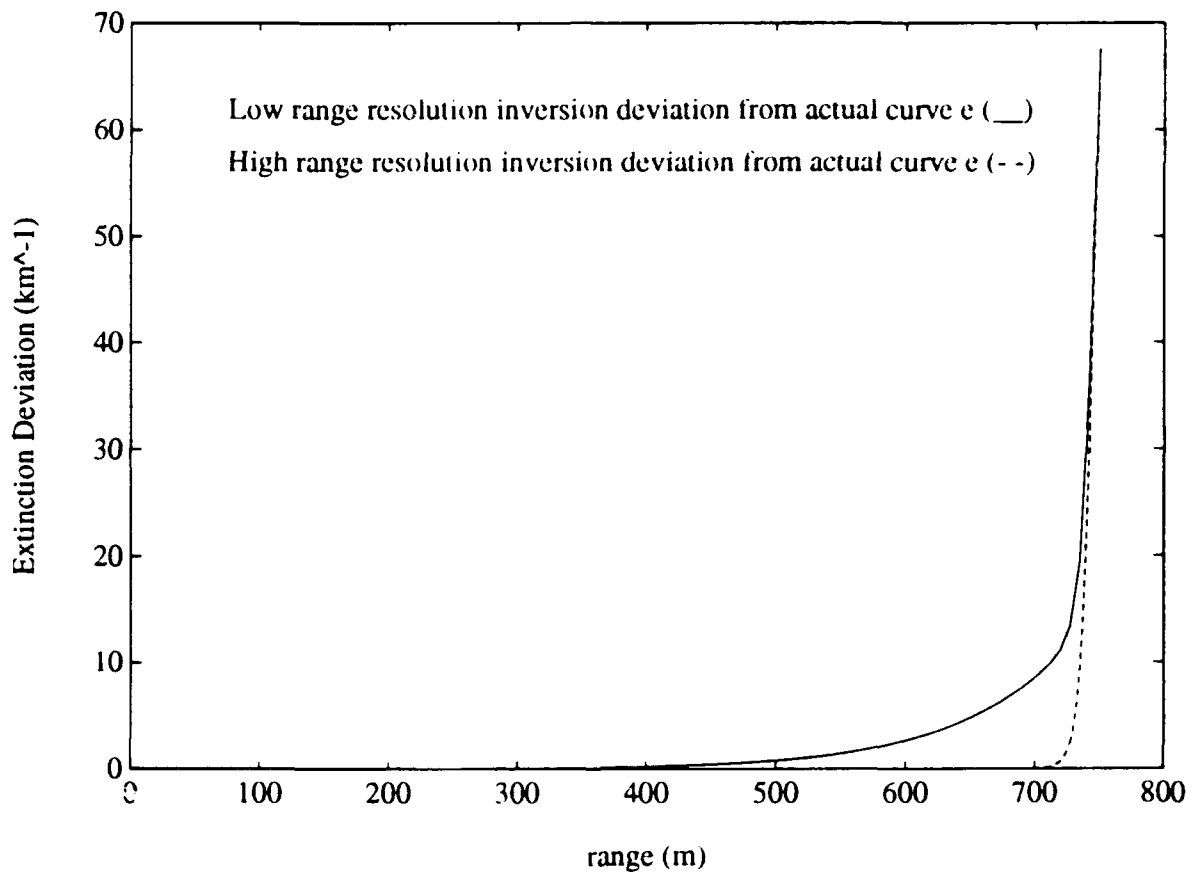

Figure 22. Extinction Coefficient deviations from the actual values (Figure 16 curve e) by the the high and low-resolution inversions.

6. Figure 23. This figure shows the difference between the low and high-resolution inversions of the S(r) file, generated from curve f from Figure 16, and the actual curve f. The large deviation noted in Figure 22 was not observed in Figure 23 which was consistent since there was a small dynamic range for the Extinction Coefficient.
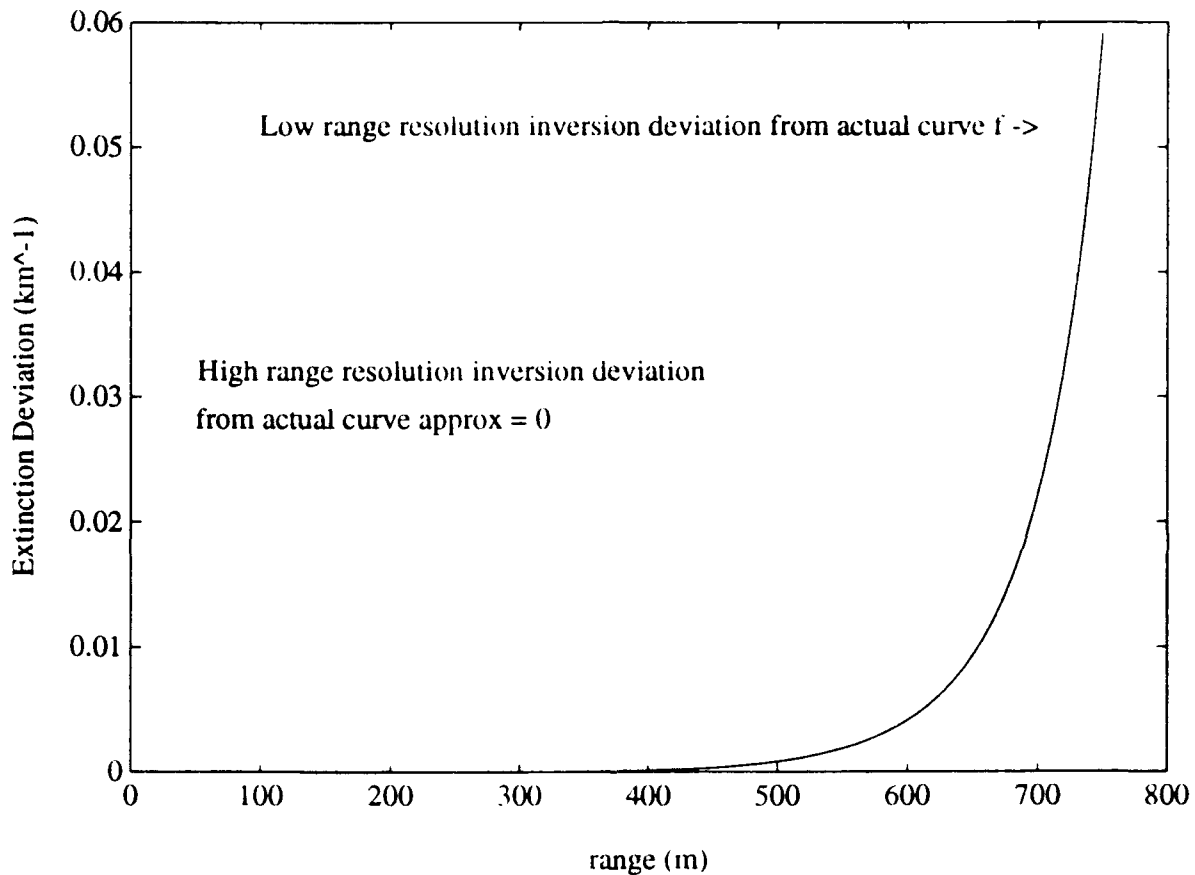

Figure 23. Extinction Coefficient deviations from the actual values (Figure 16 curve f) by the the high and low-resolution inversions.

7. Figure 24. This figure shows difference between the low and high-resolution inversions of the S(r) file, generated from curve g from Figure 17, and the actual curve g. The large deviation at 700 meter range previously described in Figure 22 for the behavior of the Low Visibility algorithm was again observed here. The effect of increasing the range resolution is to increase slightly the range from which accurate Extinction Coefficient data can be obtained.
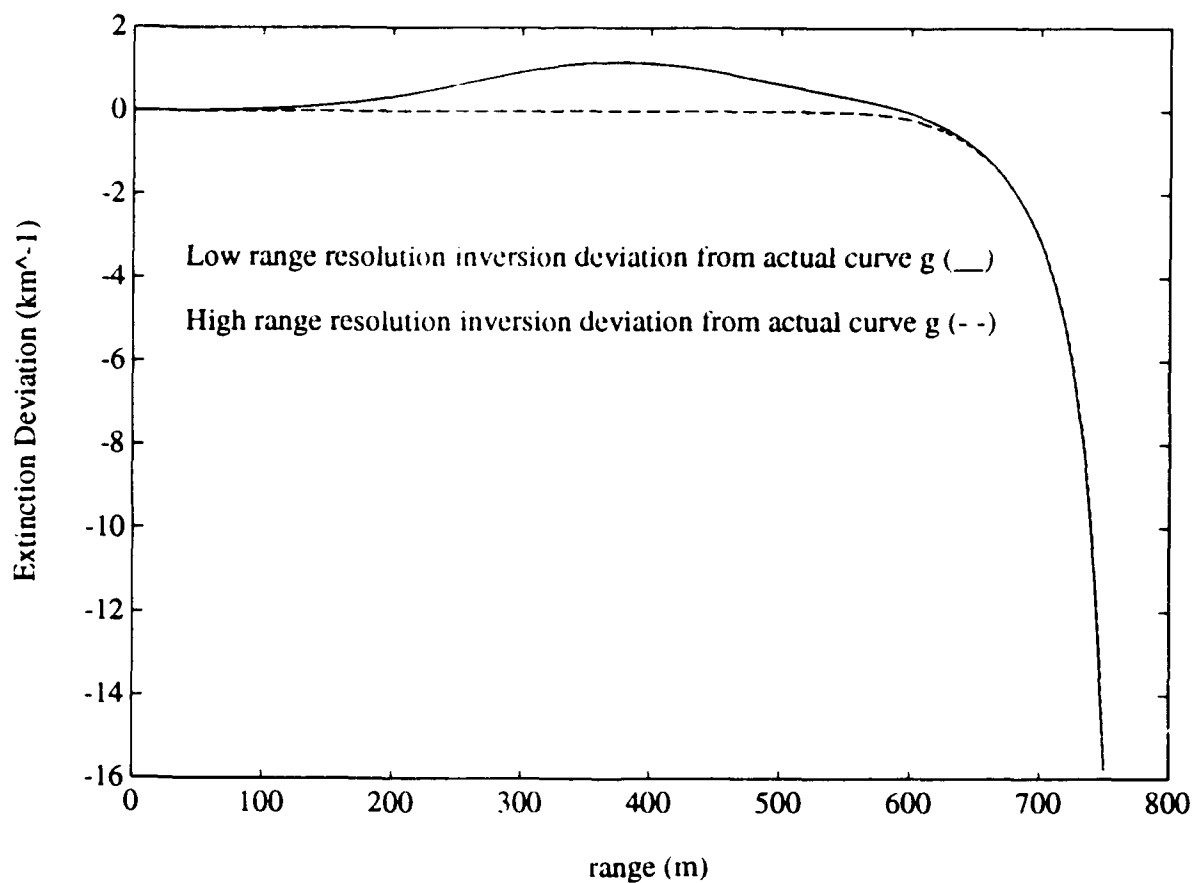

Figure 23. Extinction Coefficient deviations from the actual values (Figure 17 curve g) by the the high and low-resolution inversions.

8. Figure 25. This figure shows the difference between the low and high-resolution inversions of the $S(r)$ file, generated from curve h from Figure 17, and the actual curve h. The same lack of effect by the Low Visibility algorithm was noted. The maximum deviation is in the order of 10^{-4}.
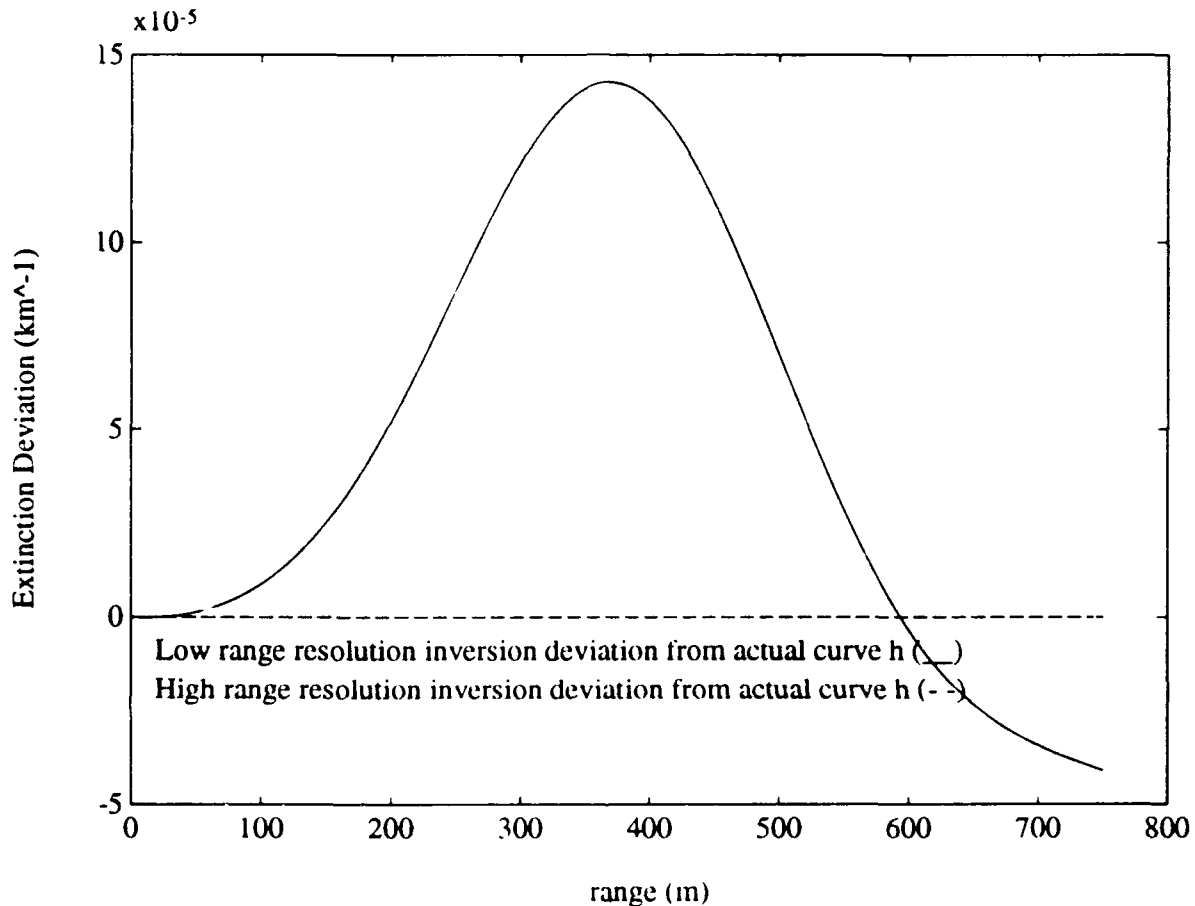

Figure 25. Extinction Coefficient deviations from the actual values (Figure 17 curve h) by the the high and low-resolution inversions.

It was not the aim of this thesis to improve the Klett algorithm. However, it may be noted that the unreliability of the Low Visibility algorithm may not be as much of a problem as first thought. The main problem occurs near the boundary range where the backscattered return will be very close to the noise floor. Therefore, the last part of the lidar inversion may not provide any useful data due to noise corruption and could be discarded.

83

The final part of the lidar inversion analysis involves the addition of noise to the received backscattered signal. The photon noise statistics are a poisson process but, in this case, since the lidar receiver observation time is long, the Central Limit Theorem can be applied. The result is that the background noise can be approximated by a Gaussian process which can be easily implemented. The total signal at the output of the receiver is a summation of the actual lidar backscattered signal $P(r)$ and the background noise power. An additive noise magnitude was arbitrarily set to 20% of the value for $P(r_m)$ in the absence of actual data.

A constant (curve a, Figure 14), dynamic range (curve h, Figure 17) and exponentially increasing (curve e, Figure 16) extinction coefficient profiles were used in the noise analysis. The exponentially decreasing extinction coefficient profile was found to have the same noise characteristics as the exponentially increasing case and was not used. The low-resolution profiles were used for the analysis because the effects were easier to observe.

The noisy inverted extinction coefficient profiles generated, from curves a, f and h, are in Figures 25, 26 and 27, respectively. There is an effect of the simulated background noise on the inversion but it influences some profiles more than others. In general, the suppression of the background noise will be important in order to reach the theoretically predicted maximum ranges of the lidar in Chapter II. There are a number of approaches, such as frequency spectrum analysis based on statistical signal processing theory and time domain analysis, which could be employed. The time analysis could easily be employed by averaging a number of lidar returns over a short period of time using the sample and average capability on the digitizing oscilloscope. This assumes that the atmosphere is relatively calm and the extinction coefficient profile is constant over a short period of time.
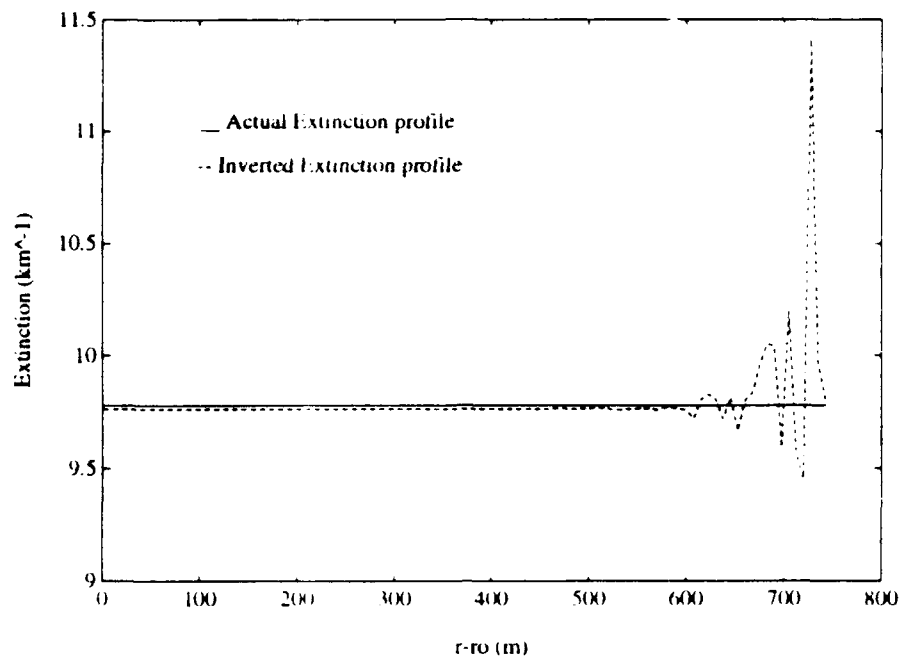
84

Figure 25. Noisy Constant Extinction Coefficient Inversion using
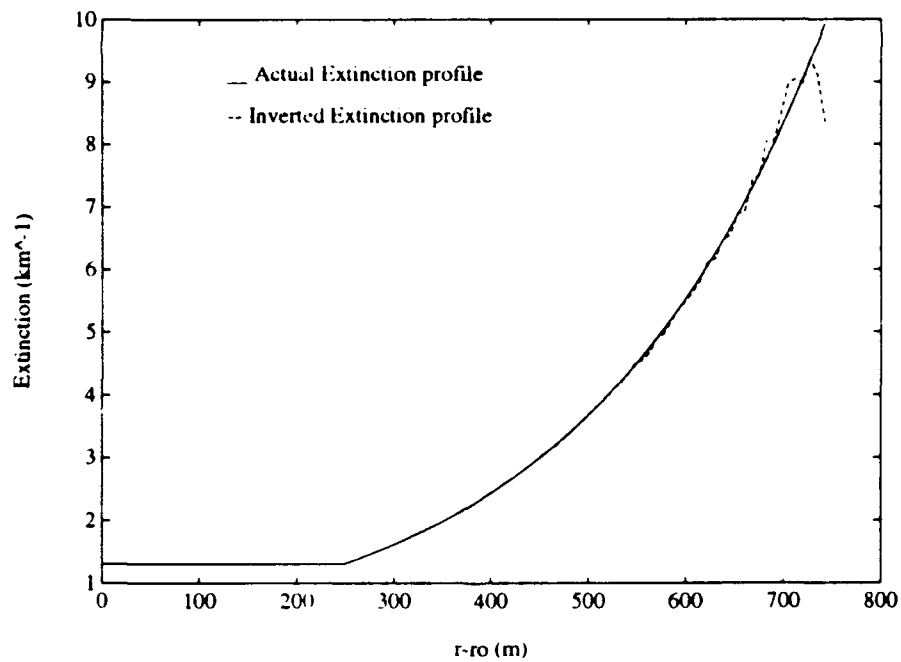Figure 14 curve *a* profile.

Figure 26. Noisy Exponentially Increasing Extinction Coefficient
Inversion using Figure 16 curve *f* profile.
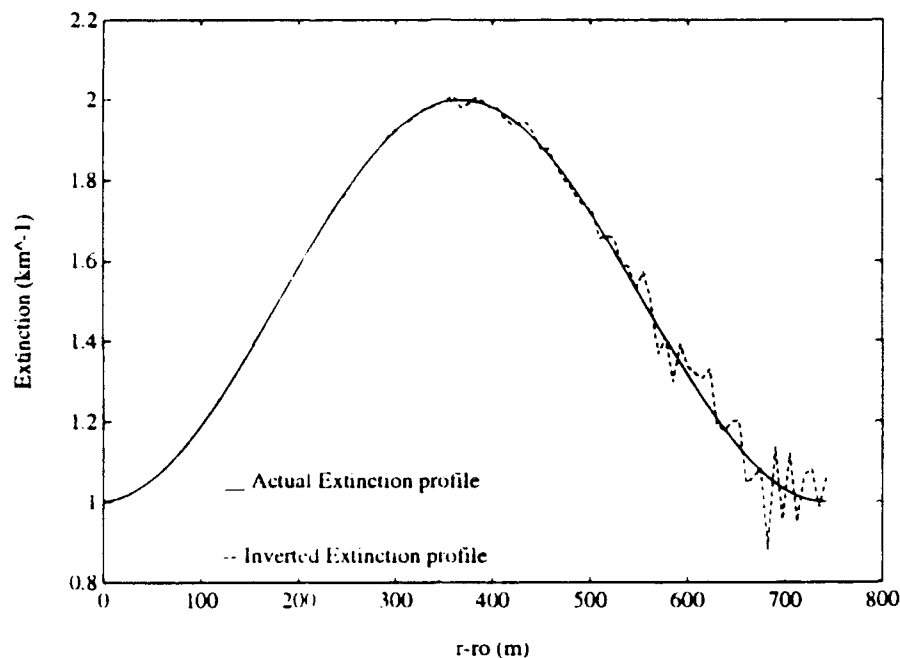
Figure 27. Noisy Dynamic Range Extinction Coefficient Inversion
using Figure 17 curve *h* profile.

D. MATLAB LIDAR INVERSION PROGRAM

This section contains the MATLAB code used to perform the lidar inversions.

```
% Theoretical Lidar Inversion of known extinction coefficient profiles
% using Klett's Technique.
% This program is robust enough to use high or low resolution (time/range data)
% Author - Major M.M. Regush
% Date - 26 May 1993


clg
clear


%
% Load Known extinction coefficient files low or high range resolution
% Constant, Exponentially Increasing/Decreasing or Dynamic
%          range extinction profiles
%
```

```
name=input('Input Data file name - ','s');
eval(['load ',name])
sigma=eval([name]);
sigma=sigma';
%     Note extinction coefficient file starts at range = r_o.
%     Therefore must add one more extinction value at the start to obtain
%     the range r = 0 to 750 meters
sigma=[sigma(1) sigma];
[p,q]=size(sigma);


% Definitions
k=1;              % power law relationship exponential between the
                  % backscattered & extinction coefficients
range=linspace(0,750,q)/1000;
[m,n]=size(range);
h=abs(range(2)-range(1));   % Range resolution


%
% Determination of S(r) - Log Adjusted Power P(r)
%
C1=1;        % Arbitrary Constant from equation (B-1)
%     Integration of Extinction Coefficient using trapezoidal rule
total=0;
for x=1:n
   total=total+sigma(x);
   sint(x)=total-.5*(sigma(x)+sigma(1));
end
sint=sint*h;
Sr=C1+k*log(sigma)-2*sint;
%     Remove the range = 0 m point as it is no longer needed
Sr=Sr(2:n);
So=Sr(1);
range=range(2:n);
ro=range(1);
sigma=sigma(2:n);
n=n-1;


%
% Noise added to the lidar backscattered return, if desired.
%
noise=input('Add simulated Gaussian background noise (y/n) -> ','s');
if noise == 'y'
   % Make P(r) file
   Pr=exp(Sr)./(range.^2);
   rand('normal')        % Gaussian distribution
   nr=rand(1,q-1);
   disp(' Arbitrarily set max noise magnitude to 20% of P(r_m) magnitude')
```

87

```
    nr=nr.*(Pr(q-1)*.2)/max(nr);
    Pr=Pr+nr;
    Sr=log(Pr.*(range.^2));  % New modified S(r) file
end


%
% Lidar Signal Inversion Analysis - sigma(r)
%
Sm=Sr(n);
rm=max(range);
%    Integration of exp(Sr-Sm)
snew=exp((Sr-Sm)/k);
total=0;
for x = 1:n
    y=n-x+1;
    total=total+snew(y);
    Sint(y)=total-.5*(snew(y)+snew(n));
end
Sint=Sint*h;
%        Boundary Value Sigma Determination
flag=0;  % Used for sigma(rm) algorithms
I=Sint(1)/(rm-ro);
Gm=(Sm-C1)/k + log(2*(rm-ro)/k);
 disp(' ')
disp('Use High Vis Algorithm to Determine sigma(rm)')
 disp(' ')
sro=0;   % Initial Condition for sigma(ro)
Gmp=Gm + 2*ro*sro/k;
% Initial Check of High Vis Algorithm
    if exp(-Gmp) <= (I+.01)
        flag=1;
    end
dsro=abs(Gm);
while dsro > .00001
    Gmp=Gm + 2*ro*sro/k;
    srm=k*.5/((rm-ro)*(exp(-Gmp)-I));
    sro1=snew(1)*srm/(1+2*srm/k*Sint(1));
    dsro=abs(sro-sro1);
    sro=sro1;
end


% Final Check Of High Vis Algorithm
if exp(-Gmp) <= (I+.01) | srm <= .01 | (sro/srm) >= 50
    flag=1;
end
```

88

```
if flag == 1 & I > 1
  disp('*** High Vis Algorithm Failed Use Low Vis Algorithm ***')
   disp(' ')
  srm1=1;        % Initial Condition for sigma(rm)
  gM=2*srm1*(rm-ro)/k;
  dgM=gM;;
  while dgM > .001
    gM1=log(1 + gM*I);
    dgM=abs(gM-gM1);
    gM=gM1;
  end
  srm=gM*k*.5/(rm-ro);      % Boundary Value sigma(rm)
elseif flag ==1 & I < 1
  disp('*** Low Visibility Algorithm Failed Use Default Algorithm ***')
   disp(' ')
  gMc=(rm-ro)/(ro*I);
  srm=gMc*k*.5/(rm-ro);     % Boundary Value sigma(rm)
end



%
%      Lidar Inversion Eqn
%
snewp=(srm^(-1)+2/k*Sint);
 sn=snew.*snewp.^(-1);



%
% Plots of S(r) file and actual & inverted extinction profile results
%
subplot(211),plot((range-ro)*1000,(Sr-So)),
title('Log Range-Adjusted Power from Extinction Coefficient Profile'),
 xlabel('r-ro (m)'),ylabel('S(r) - S(ro)')
grid
 subplot(212),plot((range-ro)*1000,sn,'--',(range-ro)*1000,sigma,'-'),
title('Actual (__) & Inverted Extinction Profiles (--) Comparison'),
 xlabel('r-ro (m)'),ylabel('Extinction (km^-1)')
grid
pause
```

```
%
% Numerical Comparisons
%
disp('Numerical Comparisons of Actual & Inverted Extinction Profiles');
fprintf('Inverted Extinction Coefficient @  rm %g  km^-1\n',srm)
fprintf('Known Extinction Coefficient @  rm %g km^-1\n',sigma(n))
sbve=(srm-sigma(n))/sigma(n)*100;
fprintf('Extinction Coefficient Boundary Value Error %g Percent \n',sbve)
fprintf('Average Inverted Extinction Coefficient %g km^-1\n',mean(sn))
fprintf('Average known Extinction Coefficient %g km^-1\n', mean(sigma))
ase=(mean(sn)-mean(sigma))/mean(sigma)*100;
fprintf('Average Extinction Coefficient Error %g Percent \n',ase)
fprintf('Delta of Extinction Coefficients @ ro %g \n', abs(sigma-sn(1)))
fprintf('Delta of Extinction Coefficients @ rm %g \n',abs(sigma(n)-sn(n)))
mdbkis=max(abs(sigma-sn));
fprintf('Max Difference between Extinction Coefficients @ %g \n',mdbkis)

% Visual Range Determination using empirical formula (see Chapter V)
 disp(' ')
disp('Determination of Visibility')
avis=3.91/mean(sigma)*(550/532)^1.3;
ivis=3.91/mean(sn)*(550/532)^1.3;
fprintf('Actual Visibility = %g km \n',avis);
fprintf('Visibility determined from Inversion Process = %g km \n',ivis);
```

LIST OF REFERENCES

1. Bernier, J.D., *Real Time Imaging and Infrared Background Scene Analysis Using the Naval Postgraduate School Infrared Search and Target Designation (NPS-IRSTD) System*, Master's Thesis, Naval Postgraduate School, Monterey, California, September 1991.

2. Hirakawa, S., *Passive Determination of Temperature and Range Using Spectral Band Measurements of Photon Emittance*, Master's Thesis, Naval Postgraduate School, Monterey, California, September 1991.

3. Payne, S.S., *Range Estimation Using Multiple Frame Infrared (IR) Images*, Unpublished Master's Thesis, Naval Postgraduate School, Monterey, California, June 1985.

4. Jarvis, R.A., "A Perspective on Range Finding Techniques for Computer Vision," *IEEE Transactions on Pattern Analysis and Machine Intelligence*, v. PAMI-5, pp. 122–138, March 1983.

5. Measures, R.M., "Atmospheric Lidar Applications" in *Laser Remote Sensing Fundamentals and Applications*, pp. 320–413, Krieger Publishing Company, Malabar, Florida, 1992.

6. Johnson, E.A., and others, "The Measurement of Light Scattered by the Upper Atmosphere from a Search Light," *Journal of Optical Society of America*, v. 29, pp. 512–517, December 1939.

7. Collis, R.T.H., "LIDAR," in *Advances in Geophysics*, v. 13, Landsberg, H.E., and Van Mieghem, J., eds, p. 114, Academic Press, New York and London, 1969.

8. Hamon, D.R., *An Analysis of LIDAR Atmospheric Remote Sensing*, Master's Thesis, Naval Postgraduate School, Monterey, California, June 1980.

9. US Army Electronics Research and Development Command, Atmospheric Sciences Laboratory Report ASL-TR-0042, *The Visioceilometer: A Portable Cloud Height and Visibility Indicator*, by R.S. Bonner and W.J. Lentz, October 1979.

10. McCartney, E.J., *Optics of the Atmosphere*, pp. 29–34, John Wiley & Sons, Incorporated, 1976.

11. Klett, J.D., "Stable Analytical Inversion Solution for Processing Lidar Returns," *Applied Optics*, v. 20, no. 2, pp. 211–220, 1981.

12. Viezee, W., Uthe, E.E., and Collis, R.T.H., "Lidar Observations of Airfield Approach Conditions: An Exploratory Study," *Journal of Applied Meteorology*, v. 8, pp. 274–283, April 1969.

13.   Ferguson, J.A., and Stephens, D.H., "Algorithm for Inverting Lidar Returns," *Applied Optics*, v. 22, no. 23, pp. 3673–3675, 1983.

14.   Mulders, J.M., "Algorithm for Inverting Lidar Returns: Comment," *Applied Optics*, v. 23, no. 17, pp. 2855–2856, 1984.

15.   Gonzalez, R., "Recursive Technique for Inverting the Lidar Equation," *Applied Optics*, v. 27, no. 13, pp. 2741–2745, 1988.

16.   Rakalski, J., Grabowski, J. and Bagienski, Z., "Novel Method for Inverting Lidar Returns," *Laser Radar III*, Becherer, R., ed., SPIE Proceeding, v. 999, pp. 208–215, 1988.

17.   Yee, E., "Information-Theoretic Method for the Inversion of the Lidar Equation," *Applied Optics*, v. 28, no. 9, pp. 1628–1637, 1989.

18.   Mitev, V.M., Grigorov, I.V., and Simenonov, V.B., "Lidar Measurements of Atmospheric Aerosol Extinction Profiles: A comparison between two techniques - Klett Inversion and Pure Rotational Raman Scattering Methods," *Applied Optics*, v. 31, no. 30, pp. 6469–6474, 1992.

19.   Klett, J.D., "Lidar Calibration and Extinction Coefficients," *Applied Optics*, v. 22, no. 4, pp. 514–515, 1983.

20.   Klett, J.D., "Extinction Boundary Value Algorithms for Lidar Inversion," *Applied Optics*, v. 25, no. 15, pp. 2462–2464, 1986.

21.   Dereniak, E., and Crowe, D.G., "Photoemissive Detector Theory" in *Optical Radiation Detectors*, pp. 113–132, John Wiley & Sons, New York, 1984.

22.   Measures, R.M., "Laser Systems as Remote Sensors" in *Laser Remote Sensing Fundamentals and Applications*, pp. 205–236, Krieger Publishing Company, Malabar, Florida, 1992.

23.   Pinnick, R.G., and others, "Backscatter and Extinction in Water Clouds," *Journal of Geophysical Research*, v. 88, pp. 6787–6796, 1983.

24.   American National Standards Institute Incorporated, *American National Standard for the Safe Use of Lasers*, ANSI Z136.1-1986, The Laser Institute of America, Orlando, Florida, 1989.

25.   Schwiesow, R.L. and others, "Aerosol Backscatter Coefficient Profiles Measured at 10.6 μm," *Journal of Applied Meteorology*, v. 20, pp. 184–194, February 1981.

26.   Edmund Scientific, *1993 Annual Reference Catalog for Optics, Science and Education*, pp. 48, 1992.

27. Telephone conversations and various facsimile transmissions between Mr. Chris Hardy, Kigre Incorporated, and Mr. William Lentz, Naval Postgraduate School, 1992.

28. Tinsley Laboratories Incorporation Letter to Professor E.G. Crittenden, Naval Postgraduate School, Subject: General Facilities Brochure and Telescope Specifications, 16 November 1973.

29. Pelco Sales Incorporated, Model PT2000L Extra Heavy Duty Pan and Tilt Specification Sheet, 1992.

30. LeCroy Corporation, Model VV100B Wideband Pulse Amplifier Specifications, June 1988.

31. Hamamatsu Corporation, *Photomultiplier Tube Catalog*, 1990.

32. Facsimile transmission from Mr Ray Muller, Hamamatsu Corporation, Western USA Office to the author, 29 April 1993.

33. Howard, N.E., *Handbook for Telescope Making*, pp. 216–219, Faber and Faber Limited, London, Great Britain, 1962.

34. Tektronix, *DSA 602A Digitizing Signal Analyzer Users Manual*, 1992.

35. Weichel, H., "Atmospheric Scattering" in *Laser Beam Propagation in the Atmosphere*, pp. 24–39, v. TT 3, SPIE Optical Engineering Press, Bellingham, Washington, 1990.

36. McCartney, E.J., *Optics in the Atmosphere*, pp. 303–318, John Wiley & Sons, New York, 1976.

37. McCartney, E.J., "Structure and Composition of the Gas Atmosphere" in *Optics of the Atmosphere*, pp. 50–113, John Wiley & Sons, New York, 1976.

38. Measures, R.M., "Propagation Through the Atmosphere" in *Laser Remote Sensing Fundamentals and Applications*, pp. 138–145, Krieger Publishing Company, Malabar, Florida, 1992.

39. Woodman, D.P., "Limitations in Using Atmospheric Models for Laser Transmission Estimates," *Applied Optics*, v. 13, no. 13, pp. 2193–2195, 1974.

40. Laser Focus World, *The Buyers Guide*, 1993.

41. National Oceanic and Atmospheric Administration, Technical Report ERL 296-WPL 29, *A Theoretical Analysis of the Information Content of LIDAR Atmospheric Returns*, by V.E. Derr and others, pp. 161–172, November 1974.

42. Arshinov, Y.F., and others, "Atmospheric Temperature Measurements Using a Pure Rotational Raman Lidar," *Applied Optics*, v. 22, no. 19, pp. 2984–2990, 1983.

43. Cooney, J., "Measurement of Atmospheric Temperature Profiles by Raman Backscatter," *Journal of Applied Meteorology*, v. 11, pp. 108–112, February, 1972.

44. Zuev, V.E., and Naats, I.E., *Inverse Problems of Lidar Sensing of the Atmosphere*, pp. 231–235, Springer-Verlin Berlin Heidelberg, 1983.

45. National Oceanic and Atmospheric Administration, Technical Report ERL 296-WPL 29, *A Theoretical Analysis of the Information Content of LIDAR Atmospheric Returns*, by V.E. Derr and others, pp. 47–66, November 1974.

46. Fiocco, G. and others, "Measurement of Temperature and Aerosol to Molecule Ratio in the Troposphere by Optical Radar," *Nature Physical Science*, v. 229, pp. 78–79, 18 January 1971.

INITIAL DISTRIBUTION LIST

1. Defense Technical Information Center   2
   Cameron Station
   Alexandria, Virginia 22314-6145

2. Library, Code 52   2
   Naval Postgraduate School
   Monterey, California 93943-5100

3. Chairman, Code EC   1
   Department of Electrical and Computer Engineering
   Naval Postgraduate School
   Monterey, California 93943-5121

4. Chairman, Code PH   1
   Department of Physics
   Naval Postgraduate School
   Monterey, California 93943-5100

5. Professor A.W. Cooper, Code PH/Cr   2
   Deparment of Physics
   Naval Postgraduate School
   Monterey, California 93943-5100

6. Professor J.P. Powers, Code EC/Po   1
   Department of Electrical and Computer Engineering
   Naval Postgraduate School
   Monterey, California 93943-5121

7. Mr. W. Lentz, Code PH/Lz   1
   Department of Physics
   Naval Postgraduate School
   Monterey, California 93943-5100

8. Directorate Scientific Information Services   1
   Research and Development Branch
   National Defence Headquarters
   Major General R. Pearkes Building
   Ottawa, Ontario
   Canada
   K1A 0K2

9. Major M.M. Regush   2
   DLAEEM 4-4
   Director General of Land Engineering and Maintenance
   National Defence Headquarters
   Major General R. Pearkes Building
   Ottawa, Ontario
   Canada
   K1A 0K2